ARTICLES
https://doi.org/10.1038/s41565-020-0696-3
nature nanotechnology

Subretinally injected semiconducting polymer nanoparticles rescue vision in a rat model of retinal dystrophy

José Fernando Maya-Vetencourt[1,2,3], Giovanni Manfredi[4], Maurizio Mete[5], Elisabetta Colombo[1,2], Mattia Bramini[1,12], Stefano Di Marco[1,2], Dmytro Shmal[1], Giulia Mantero[1], Michele Dipalo[6], Anna Rocchi[1,2], Mattia L. DiFrancesco[1], Ermanno D. Papaleo[1], Angela Russo[5], Jonathan Barsotti[4], Cyril Eleftheriou[1,13], Francesca Di Maria[7], Vanessa Cossu[2,8], Fabio Piazza[9], Laura Emionite[2], Flavia Ticconi[2,8,14], Cecilia Marini[10], Gianmario Sambuceti[2,8], Grazia Pertile[5], Guglielmo Lanzani[4,11] ✉ and Fabio Benfenati[1,2] ✉

Inherited retinal dystrophies and late-stage age-related macular degeneration, for which treatments remain limited, are among the most prevalent causes of legal blindness. Retinal prostheses have been developed to stimulate the inner retinal network; however, lack of sensitivity and resolution, and the need for wiring or external cameras, have limited their application. Here we show that conjugated polymer nanoparticles (P3HT NPs) mediate light-evoked stimulation of retinal neurons and persistently rescue visual functions when subretinally injected in a rat model of retinitis pigmentosa. P3HT NPs spread out over the entire subretinal space and promote light-dependent activation of spared inner retinal neurons, recovering subcortical, cortical and behavioural visual responses in the absence of trophic effects or retinal inflammation. By conferring sustained light sensitivity to degenerate retinas after a single injection, and with the potential for high spatial resolution, P3HT NPs provide a new avenue in retinal prosthetics with potential applications not only in retinitis pigmentosa, but also in age-related macular degeneration.

The progressive degeneration of retinal photoreceptors is one of the most frequent causes of severe visual impairment in developed and ageing populations. The two most prevalent retinal degenerative diseases are age-related macular degeneration (AMD) and retinitis pigmentosa (RP)[1]. RP, a collective name for a set of genetic disorders that cause death of rods and secondarily of cones, afflicts 1 in 4,000 people worldwide and is the most common inherited retinal degeneration, while the atrophic form of AMD affects about 1.4–20% of the population aged between 70 and 90 years worldwide and primarily targets foveal cones[2]. Gene supplementation, optogenetic or stem cell therapies for these diseases are very promising, but except for the commercially available gene therapy for RPE65-linked retinal dystrophy, are still in preclinical experimentation or early phases of human testing[3–5]. Thus, several groups have tried to rescue vision by electrically stimulating the preserved inner retinal circuits with epiretinal, subretinal or suprachoroidal prosthetic implants[6–11].

Organic semiconductors have been introduced as interfaces for neuronal photostimulation in retinal prostheses[12–14]. In such devices, a conjugated-polymer (such as poly[3-hexylthiophene], P3HT) layer is contacted on one side by an underlying conductive layer (indium tin oxide or PEDOT:PSS, poly(3,4-ethylenedioxythiophene) polystyrene sulfonate), and bathed on the opposite side by the electrolytic extracellular medium[15–18]. When such a device, layered onto a silk fibroin support, was implanted in the subretinal space of dystrophic Royal College of Surgeons (RCS) rats, a widely recognized model of RP[19], it promoted a persistent conjugated-polymer-dependent rescue of vision that lasted up to 6–10 months after implantation with sensitivity in the daylight range and high biocompatibility[20,21].

High-resolution sampling of retinal images relies on the mosaic of foveal cones about 4–5 µm in diameter that generate the dedicated midget system and provide the vast majority of the input to the visual cortex[22]. However, all the existing two-dimensional prosthetic approaches give a spatial resolution over one order of magnitude lower that that allowed by foveal cones. To circumvent these problems, we exploited the huge potential of multifunctional nanoscale materials[23–27]. We engineered P3HT nanoparticles (NPs)[28,29] as light-sensitive interfaces with retinal neurons. We find that P3HT NPs of ≈300 nm in diameter remain extracellular, and endow inner retinal neurons with light sensitivity. When microinjected in the eye of RCS rats, P3HT NPs widely and persistently distribute in the whole subretinal space, in the absence of trophic effects on residual photoreceptors or substantial inflammatory reactions. P3HT NPs

[1]Centre for Synaptic Neuroscience and Technology, Istituto Italiano di Tecnologia, Genoa, Italy. [2]IRCCS Ospedale Policlinico San Martino, Genoa, Italy. [3]Department of Biology, University of Pisa, Pisa, Italy. [4]Centre for Nano Science and Technology, Istituto Italiano di Tecnologia, Milan, Italy. [5]Ophthalmology Department, IRCCS Ospedale Sacro Cuore Don Calabria, Negrar, Italy. [6]Plasmon Nanotechnologies, Istituto Italiano di Tecnologia, Genoa, Italy. [7]CNR Institute of Organic Synthesis and Photoreactivity (ISOF), Bologna, Italy. [8]Department of Health Science, Nuclear Medicine, University of Genoa, Genoa, Italy. [9]ENT Department, ASST Mantova, Mantua, Italy. [10]CNR Institute of Bioimages and Molecular Physiology, Milan (Genoa Section), Genoa, Italy. [11]Department of Physics, Politecnico di Milano, Milan, Italy. [12]Present address: Department of Applied Physics, University of Granada, Granada, Spain. [13]Present address: Departments of Ophthalmology and Neurology, Weil Medical College of Cornell University, White Plains, NY, USA. [14]Present address: Department of Oncohematology, Nuclear Medicine Unit, Faenza Hospital, Faenza, Italy. ✉e-mail: guglielmo.lanzani@iit.it; fabio.benfenati@iit.it

rescue light-driven behaviours, visual cortex activity and visual acuity to levels indistinguishable from those of healthy congenic rats for up to 8 months after a single injection. The results indicate that P3HT NPs represent a promising approach to the treatment of both RP and AMD because of the low-invasion surgery, the permanence of the effects and the potential for high spatial resolution.

Photostimulation of retinal neurons by P3HT NPs

To ascertain whether the conductive layer in the planar organic prosthesis is needed to elicit in vivo effects, we fabricated a planar device in which P3HT was directly layered onto a passive polyethylene terephthalate (PET) substrate and implanted it in the subretinal space of RCS rats. P3HT-implanted animals showed a substantial increase in the amplitude of visually evoked potentials (VEPs) in the primary visual cortex (V1) 30 d after surgery with respect to sham-operated RCS rats (Supplementary Fig. 1), demonstrating that the photoactive polymer directly mediates the biostimulation. Thus, we proceeded to generate P3HT NPs following recently reported procedures[28,29].

Sterile P3HT NPs were prepared using the reprecipitation technique, in which nucleation of NPs is triggered by a rapid change in solvent polarity favouring π–π stacking and hydrophobic interactions. P3HT NPs were sorted by differential centrifugation, while size-matched glass NPs were used as a control (sham). The shape of P3HT NPs, analysed by scanning electron microscopy (SEM; Fig. 1a), ranged from spherical to elliptic and their size distribution, assessed by dynamic light scattering (DLS), overlapped with that of the more homogeneous spherical glass NPs (*Z*-average = 304 nm versus 254 nm of glass NPs) with low dispersity indexes (Supplementary Fig. 2). Next, we verified that P3HT NPs were not endocytosed by neurons. Indeed, P3HT NPs displayed a very low degree of colocalization with the lysosome-specific marker LAMP1 up to 7 d of incubation and finely decorated the neuronal membrane all along the processes, positioning them at the very site of action for neurostimulation (Extended Data Fig. 1). Confocal fluorescence microscopy, SEM and cross-section SEM on primary neurons plated onto a drop-cast layer of P3HT NPs showed that neurons engulfed NPs without internalizing them, thus creating an intimate contact between the NP surface and the neuronal membrane, with a quasi-virtual (<20 nm) cleft secluded from the extracellular fluid (Fig. 1b).

We tested the ability of the NP–membrane interface to induce light-dependent neuronal activation in blind retina explants from 12–14-month-old RCS rats. Patch-clamped retinal ganglion cells (RGCs) puffed with P3HT NPs and exposed to light stimuli (40 mW mm^{-2}; 500 ms) displayed a robust depolarization time-locked with the light stimulus, followed by deterministic firing (Fig. 1c,d). To mimic in vivo experiments, we next microinjected P3HT NPs into the subretinal space of blind retina explants from 12–14-month-old RCS rats. P3HT NPs triggered a light-dependent RGC firing that was completely absent from retinas injected with glass NPs (Fig. 1e). Firing induced by P3HT-NPs was characterized by a longer latency (≈300 ms) with respect to age-matched healthy retinal explants (Fig. 1f), probably due to the marked rewiring of the aged RCS retinas[30] and consistent with the in vivo latencies of cortical responses to light (see below).

Photoinduced heating can contribute to photostimulation at high powers and under conditions of limited heat dissipation (such as with P3HT films[16,31]). However, simulations of P3HT NPs dispersed in water under the conditions used for the experiments indicate a negligible temperature increase, in the millikelvin range (Supplementary Information). Alternatively, it has been demonstrated that, upon photoexcitation, negative charges are generated at the polymer/electrolyte surface[15,17,32]. The amount of charge that can be accumulated is of the order of nanocoulombs per square centimetre. Considering the low area coverage of NPs in ex vivo experiments (5×10^5 NPs cm^{-2}; Supplementary Information), the generated current is microamperes per square centimetre, orders of magnitude lower than the values needed to open voltage-dependent conductances[12]. We also demonstrated that the local concentration of cations such as H^+ and/or Na^+ is not markedly changed, since no significant light-dependent changes in heat- and pH-sensitive TRPV1 and ASIC1a currents or in the cell volume were observed in HEK293 cells plated onto P3HT NPs (Supplementary Figs. 3 and 4). Moreover, the light-induced firing activation in blind retina explants was unaffected by blockers of TRPV or ASIC1a channels (Supplementary Fig. 5). Given these negative results, we considered the capacitive mechanism that

Fig. 1 | P3HT NPs form a tight seal with the neuronal membrane and trigger light-evoked neuronal stimulation through a capacitive mechanism. a, SEM images of P3HT NPs generated with the reprecipitation method and control glass NPs of similar size. P3HT NPs are sized by differential centrifugation and DLS as shown in Supplementary Fig. 2. **b**, Top: lateral projection of confocal *z*-stack fluorescence images of calcein-labelled primary neurons layered on coverslips drop-cast with P3HT NPs. NPs (intrinsic red fluorescence) are visibly engulfed by the neuronal cell bodies and processes. Bottom: ultrastructural analysis of neuron–NP interactions before and after sectioning of standard SEM preparations (left) and of resin-embedded focused ion beam (FIB) cross-sections (right). The results are representative of $n = 3$ independent neuronal preparations. NPs establish a very tight (<20 nm) contact with the neuronal junctional membrane, with a quasi-virtual cleft secluded from the extracellular space. **c**, Left: example of a light-stimulated (green spot) patched RGC puffed with P3HT NPs. Right: representative averaged current-clamp traces (mean ± s.d.; holding current, $I_{holding} = 0$ pA) of an RGC from a 12–14-month-old RCS retina in the presence of P3HT NPs in response to 540-nm flashes (40 mW mm^{-2}, 500 ms). The results are statistically analysed in **d**. **d**, Left: peristimulus time histogram of the firing activity (mean ± s.e.m.). Right: box plots of the RGC membrane potential in the dark and after light stimulation ($n = 5$ RCS rats; $^*P < 0.05$, Wilcoxon's one-tailed test). **e**, Left: schematic representation of a blind retinal explant with the RGC layer facing the microelectrode array (MEA) and the subretinal NP injection under the choroid. Green arrows represent the direction of the light stimuli. Middle: representative raster plots of the overall firing activity of RGCs in the presence of either P3HT NPs or glass NPs (500-ms light stimulation, 40 mW mm^{-2} @ 540 nm). Right: percentage of light-evoked variation in firing of the recorded RGCs with respect to the baseline normalized to the firing in the absence of NPs. In the dose–response plot of the normalized firing activity, only neurons displaying a significant (two-sided Student's *t*-test) light-induced firing modulation with respect to the baseline were considered. $^*P < 0.05$, $^{****}P < 0.0001$, two-way analysis of variance (ANOVA)/Fisher's least significant difference tests. P3HT NPs, 35, 55, 112, 224 neurons/21 retinas; glass NPs, 25, 38, 83, 167 neurons/18 retinas; control, 21, 44, 91, 192/19 retinas for 1, 7, 18, 40 mW mm^{-2} stimuli, respectively. Data in **d**,**e** are mean ± s.e.m. **f**, The latency of ON responses in RCS-rdy retinas and P3HT-mediated ON-like responses in RCS retinas was measured in 12–14-month-old rats as the time needed to reach the peak firing rate with respect to the stimulus onset. $^{****}P < 0.0001$, two-sided Student's *t*-test ($n = 52$ neurons/15 non-injected RCS-rdy retinas and $n = 207$ neurons/10 RCS injected retinas). Box plots in **d**,**f** represent the median (centre line), mean (square), 25th–75th percentiles (box) and limit of three times the interquartile range. **g**, A schematic diagram of an NP engulfed by the neuronal membrane with the current paths and the NP–cell membrane equivalent circuit. **h**, Left: simulated junctional and extrajunctional membrane voltage variation upon 50-ms light pulse at 40 mW mm^{-2} for an interface of a single P3HT NP of 200-nm radius, using the fit parameters reported in Supplementary Information. The polarity of the potential change in the cleft is opposite to the extrajunctional one. Right: junctional and extrajunctional membrane potential peak variation as a function of the cleft resistance plot. For exact *P* values, see Supplementary Table 3.

relies on the close contact between NPs and the very high electrical resistance of the cleft, reminiscent of what has been found for mushroom-shaped electrodes[33,34] or nanopillars[35]. We designed a model to capture the NP–cell coupling, assuming the experimentally determined cleft maximum thickness of 20 nm (Fig. 1g; see Supplementary Table 1 and Supplementary Information for a complete description). We found that a junctional membrane resistance of >1 MΩ is associated with a change in membrane potential of >1 mV (Fig. 1h). Such small photopotentials, which, similar to postsynaptic potentials in central synapses, are evoked in adjacent sites and repeated in time, will summate both spatially and temporally to build up a substantial depolarization.

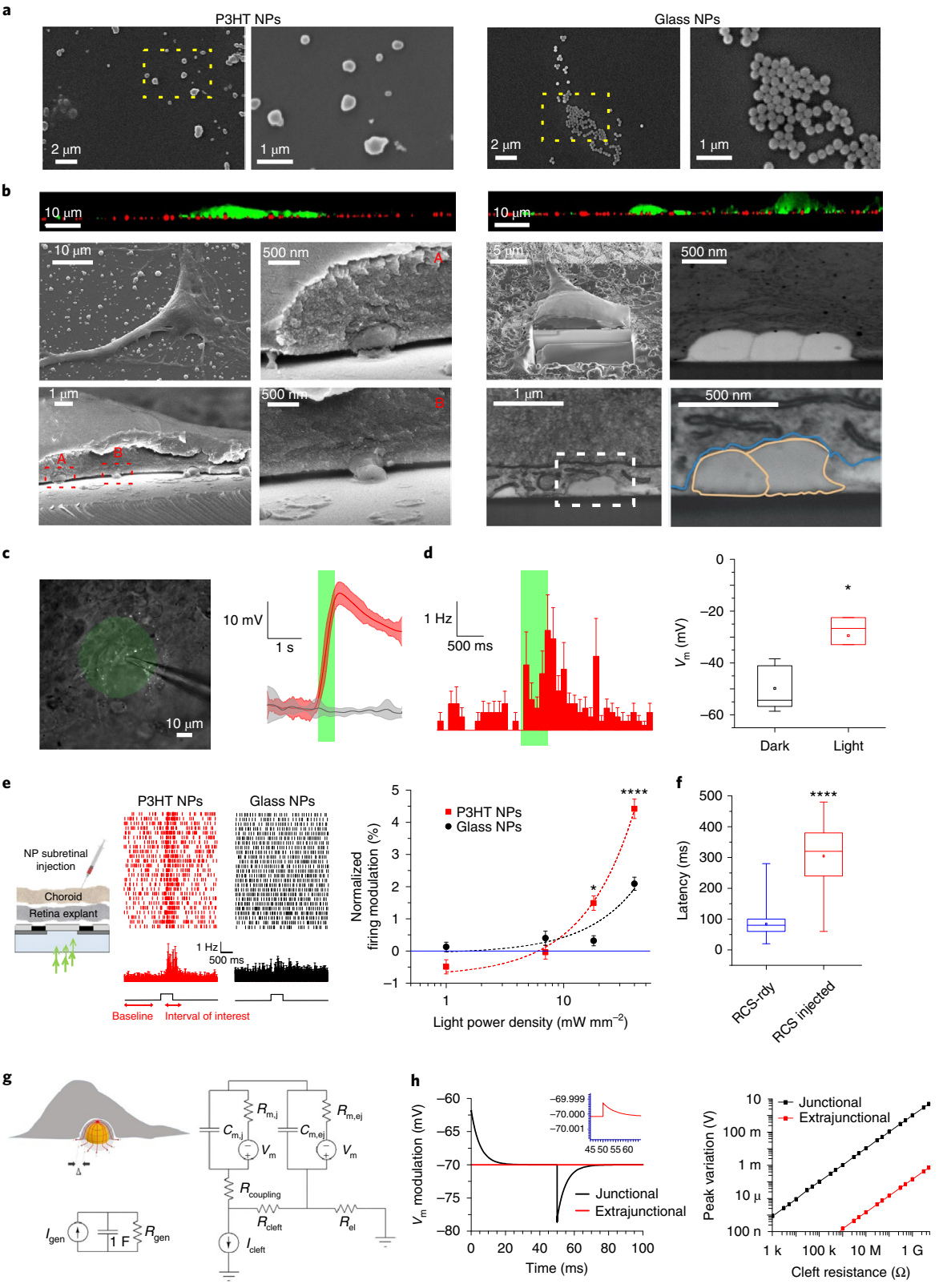

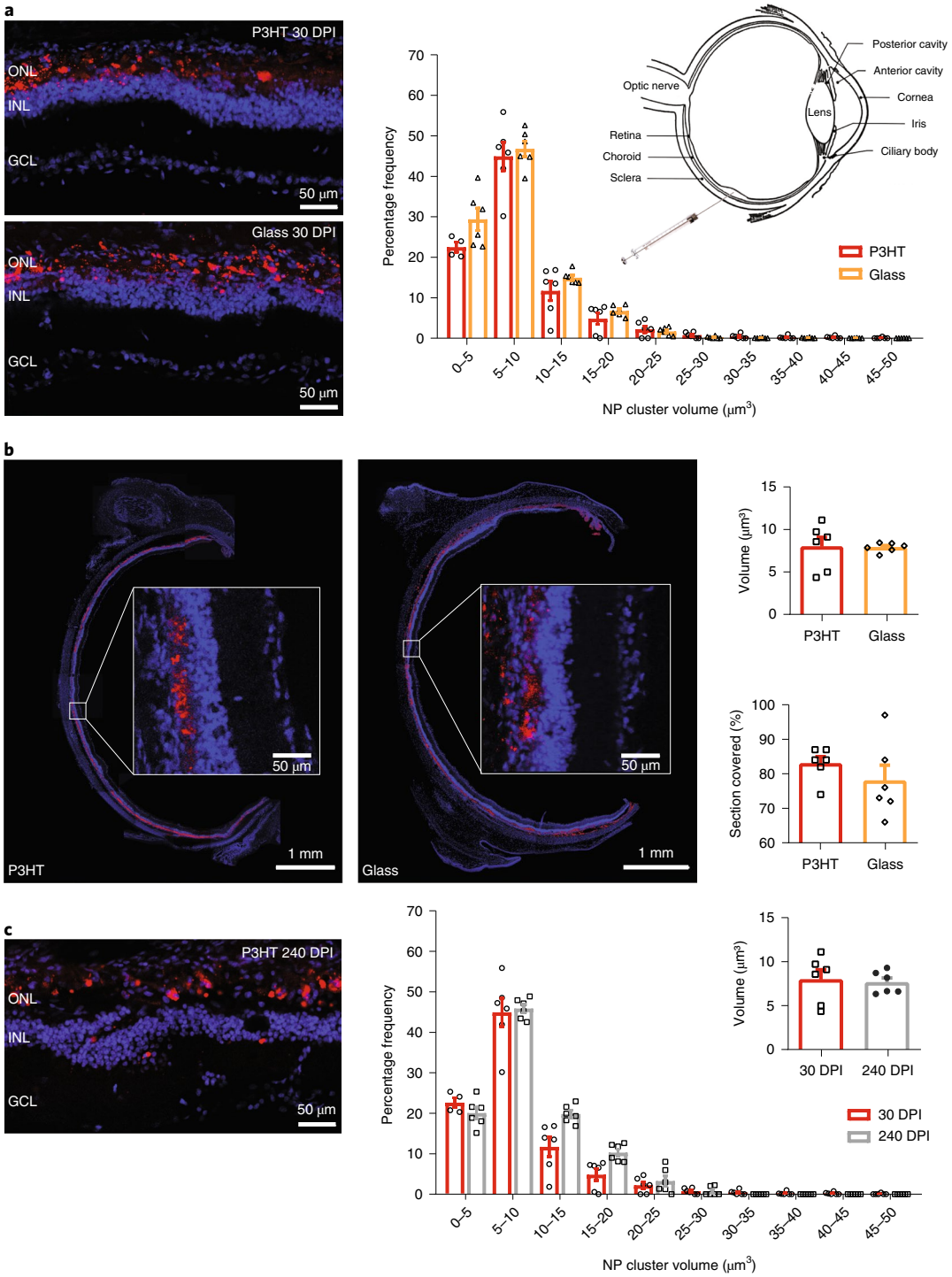

Fig. 2 | Subretinally microinjected P3HT NPs display wide and stable retina coverage and are not cleared over time. a, Left: transversal retinal sections from dystrophic RCS rats injected with either endogenously fluorescent P3HT NPs or fluorescent glass NPs at 30 DPI. NP fluorescence (red) was merged with bisbenzimide nuclear staining (blue). Right: percentage frequency distribution of the volume of P3HT and glass NP clusters (5-µm bins) at 30 DPI. The analysis was performed on *z*-stack confocal microscopy images of retinal sections (50-µm thickness) by a custom-generated macro running with ImageJ. $P > 0.10$, two-sided Kolmogorov–Smirnov test. GCL, ganglion cell layer. Inset: schematic representation of the subretinal microinjection procedure (for further details, see Methods). **b**, Left: full equatorial reconstruction of dystrophic retinas from RCS rats injected with either endogenously fluorescent P3HT NPs or fluorescent glass NPs at 30 DPI, showing the tangential diffusion of NPs (red) in the whole subretinal space, with no tendency to permeate the internal retinal layers (insets at higher magnification). Right: bar plots of the total NP volume in the subretinal space and the percentage retinal coverage for P3HT NPs or fluorescent glass NPs at 30 DPI. Individual experimental points are superimposed. $P > 0.05$, two-sided Mann–Whitney *U*-test. **c**, Left: transversal retinal section from a dystrophic RCS rat injected with P3HT NPs at 240 DPI. Middle: comparison of the percentage frequency distribution of the P3HT-NP cluster volume (5-µm bins) at 30 and 240 DPI. The analysis was performed as in **a**. $P > 0.10$, two-sided Kolmogorov–Smirnov test. Right: total P3HT-NP volume in the subretinal space at 30 and 240 DPI. Individual experimental points are superimposed. $P > 0.05$, Mann–Whitney *U*-test. Data are mean ± s.e.m. of $n = 6$ RCS rats for each experimental group (P3HT NPs 30 DPI; glass NPs 30 DPI; P3HT NPs 240 DPI). For exact *P* values, see Supplementary Table 3.

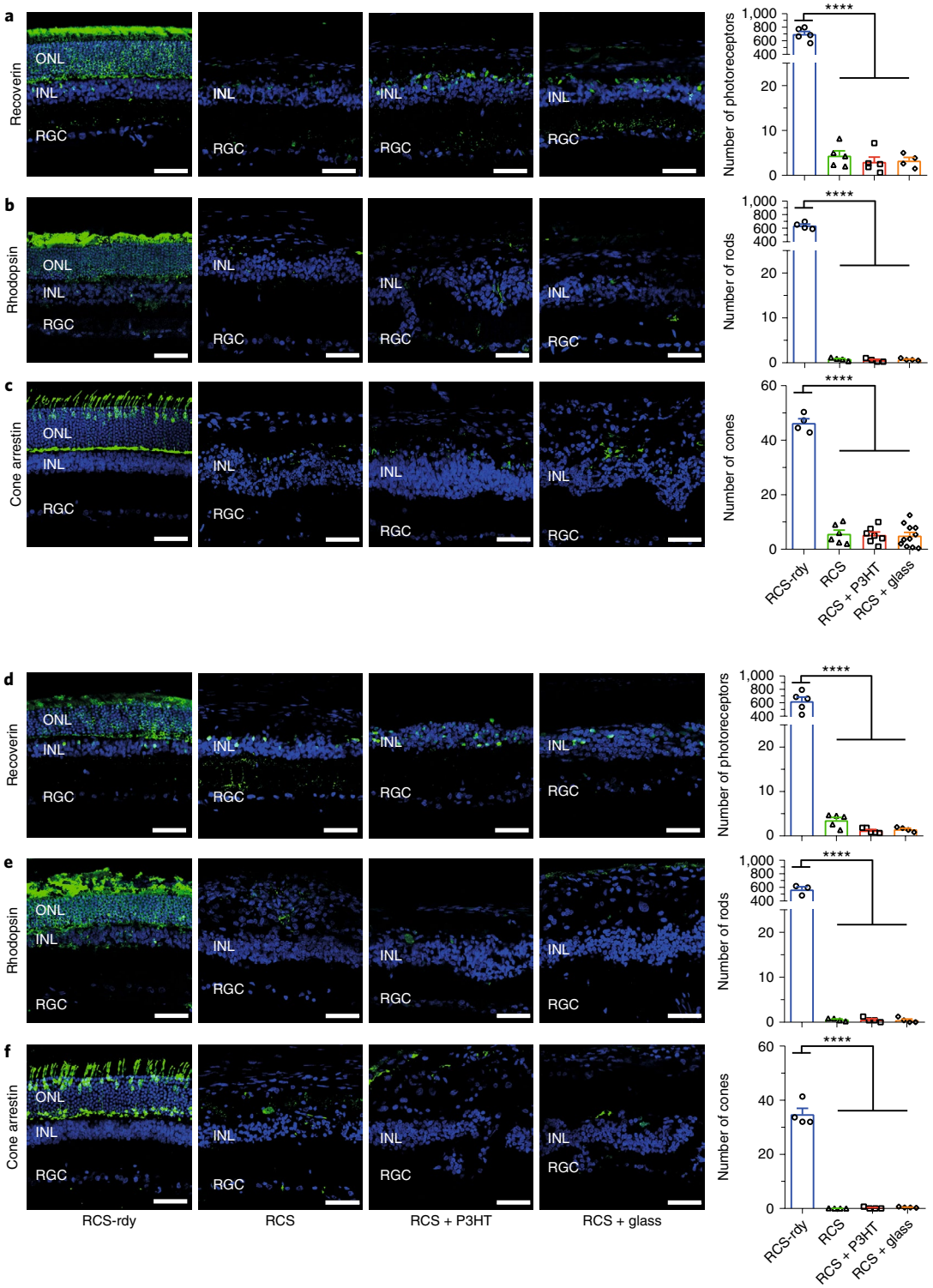

Fig. 3 | P3HT NPs do not promote photoreceptor survival in dystrophic retinas. a–f, Transversal sections of representative retinas were dissected at 30 DPI (**a**–**c**) and 240 DPI (**d**–**f**) from non-dystrophic controls (RCS-rdy), untreated dystrophic RCS rats (RCS) or dystrophic RCS rats injected with either P3HT NPs (RCS + P3HT) or control glass NPs (RCS + glass). Sections were immunolabelled for the rod/cone marker recoverin (**a**,**d**; labelling rods, cones and on/off cone bipolar cells), rhodopsin (**b**,**e**; labelling rods) and cone arrestin (**c**,**f**; labelling cones). Images were acquired from corresponding fields in the various retinas by taking the injection site as the reference point (two slices per retina; three fields per slice). The bar plots on the right (mean ± s.e.m. with superimposed individual data points) report the respective photoreceptor cell body counts. $^{****}P < 0.0001$ versus RCS-rdy controls; one-way ANOVA/Tukey tests. Sample size (experimental animals) at 30 DPI: recoverin, 5, 5, 5, 4; rhodopsin, 4, 4, 4, 4; cone arrestin, 4, 6, 7, 11 for RCS-rdy, RCS, RCS + P3HT and RCS + glass, respectively. Sample size (experimental animals) at 240 DPI: recoverin, 5, 5, 5, 4; rhodopsin, 3, 4, 4, 4; cone arrestin, 4, 4, 4, 4 for RCS-rdy, RCS, RCS + P3HT and RCS + glass, respectively. Dystrophic retinas display a very low density of photoreceptors that is not minimally affected by surgery- and/or NP-mediated trophic effects. In each panel, representative immunolabelled sections from non-injected healthy RCS-rdy rats and dystrophic RCS rats are shown merged with bisbenzimide staining for cell nuclei (blue). Scale bars, 50 μm. For exact *P* values, see Supplementary Table 3.

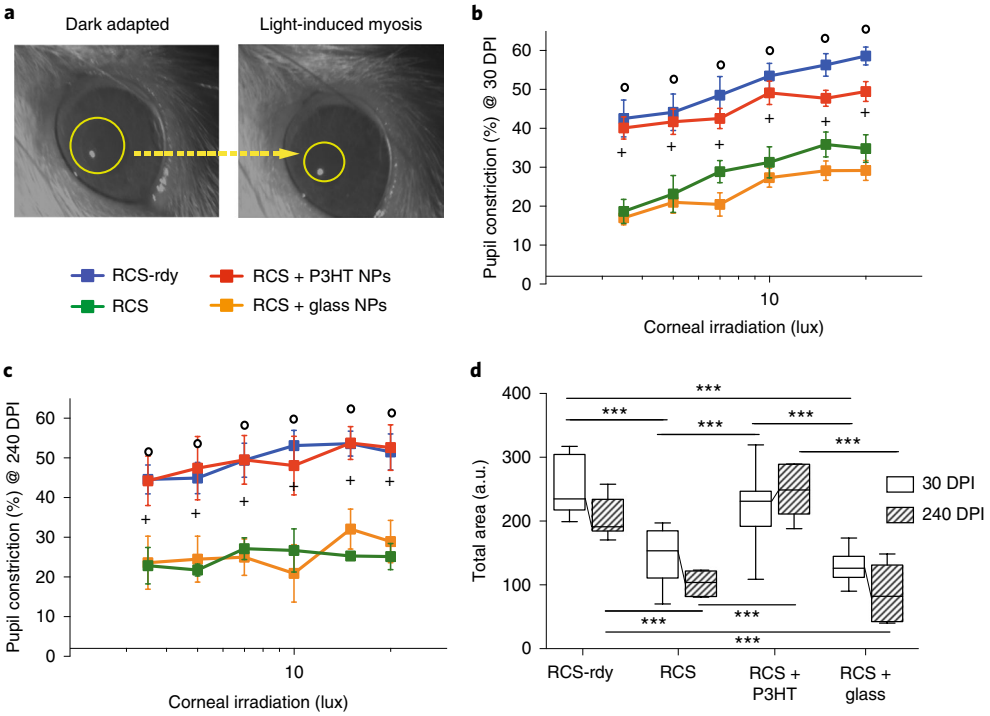

Fig. 4 | Long-term rescue of PLR in dystrophic RCS rats injected with P3HT NPs. a, Constriction of the pupil by light pulses as assessed using standard infrared imaging in dark-adapted RCS-rdy rats. **b**,**c**, Quantification of the pupillary constriction as a function of light intensity in RCS-rdy, RCS, RCS + P3HT NPs and RCS + glass NPs rats. A full recovery of the reflex even at the lowest light intensities is observed in RCS rats injected with P3HT NPs at both 30 (**b**) and 240 (**c**) DPI. Data are mean ± s.e.m. **b**, °$0.01 < P < 0.001$ RCS-rdy versus RCS; $^{+}P < 0.0001$ P3HT-NP RCS versus glass-NP RCS; **c**, °$0.01 < P < 0.001$ RCS-rdy versus RCS; $^{+}0.05 < P < 0.01$ P3HT-NP RCS versus glass-NP RCS; repeated measures ANOVA. No differences were found between RCS-rdy and RCS injected with P3HT NPs. **d**, Box plots of the areas under the light dose–response curves at 30 (open boxes) and 240 (dashed boxes) DPI for the four experimental groups. a.u., arbitrary units. While a decay of pupillary responses (lines joining the median values) is observed with age in RCS-rdy, RCS and RCS injected with glass NPs due to the progressive photoreceptor loss, RCS rats injected with P3HT NPs fully preserved the improvement in pupillary reactivity up to 240 DPI. Box plots represent the median (centre line), 25th–75th percentiles (box) and limit of three times the interquartile range. ***$P < 0.001$, one-way ANOVA/Tukey tests. Sample sizes (experimental animals): RCS-rdy, $n = 8$ and 7; RCS, $n = 11$ and 6; RCS + P3HT NPs, $n = 24$ and 6; RCS + glass NPs, $n = 18$ and 8 for 30 and 240 DPI, respectively. For exact *P* values, see Supplementary Table 3.

Subretinal P3HT NPs do not trigger trophic or proinflammatory effects

Suspensions of P3HT NPs were bilaterally injected in the subretinal space through a 38-gauge needle inserted tangentially between retina and retinal pigment epithelium in the superior temporal quadrant (Fig. 2a). The transient complete retinal detachment was confirmed by ophthalmoscopy immediately after the procedure. In vivo optical coherence tomography, performed 30 and 240 days post injection (DPI), confirmed the absence of retinal lesions or detachments, indicating that the retina spontaneously reattached to the choroid thanks to the osmotic pumping of the retinal pigment epithelium (Supplementary Fig. 6).

Both P3HT NPs and fluorescent glass NPs remained confined to the outer retina, in place of degenerated photoreceptors, and covered most of the subretinal space (Fig. 2a,b). Morphometric analysis of *z*-stack confocal microscopy images revealed that P3HT NPs and fluorescent glass NPs were organized in clusters of very similar size distribution in ventral, central and dorsal retina, with the highest frequency at a volume range of 5–10 μm^3 and an overall retinal coverage of about 80% (Fig. 2a,b and Supplementary Fig. 7). Subretinal NPs can in principle be cleared by microglia or by the choroid circulation over time. However, we found a full persistence of P3HT NPs at 240 DPI, with only minor changes in their cluster size distribution with respect to 30 DPI (Fig. 2c).

It has been reported that surgical manipulations of the retina in the pigmented RCS rats can lead to an increased survival of degenerating photoreceptors[36–39]. Thus, we investigated whether the injection of either P3HT or glass NPs non-specifically enhanced photoreceptor survival in our 3-month-old pink-eyed albino RCS rats. We first analysed the thickness of the avascular outer nuclear layer (ONL) at both 30 and 240 DPI by staining retinal and choroidal vessels. At 30 DPI, the outer retina of RCS rats already displayed a complete derangement with markedly decreased thickness, invasion by retinal vessels and broadening of the inner nuclear layer (INL). These changes were independent of whether the RCS rats had been non-injected or injected with either P3HT or glass NPs, and confirm the fast photoreceptor degeneration reported in the pink-eyed RCS strain at the same age[40]. A qualitatively similar, but more severe, picture was observed in 240-DPI retinas, in which the ONL was virtually absent. Counting of the cell body rows revealed that virtually all RCS retinas at 30 DPI had a greatly (80–85%) decreased number of cell rows in the ONL with respect to healthy retinas, which was further reduced to <10% of the healthy values at 240 DPI (Extended Data Fig. 2).

We next used photoreceptor-specific markers to dissect the combined effects of surgery and NP injection on photoreceptor survival at 30 and 240 DPI. Rod and cone cell bodies were individually labelled with rhodopsin or cone-arrestin antibodies, respectively, or

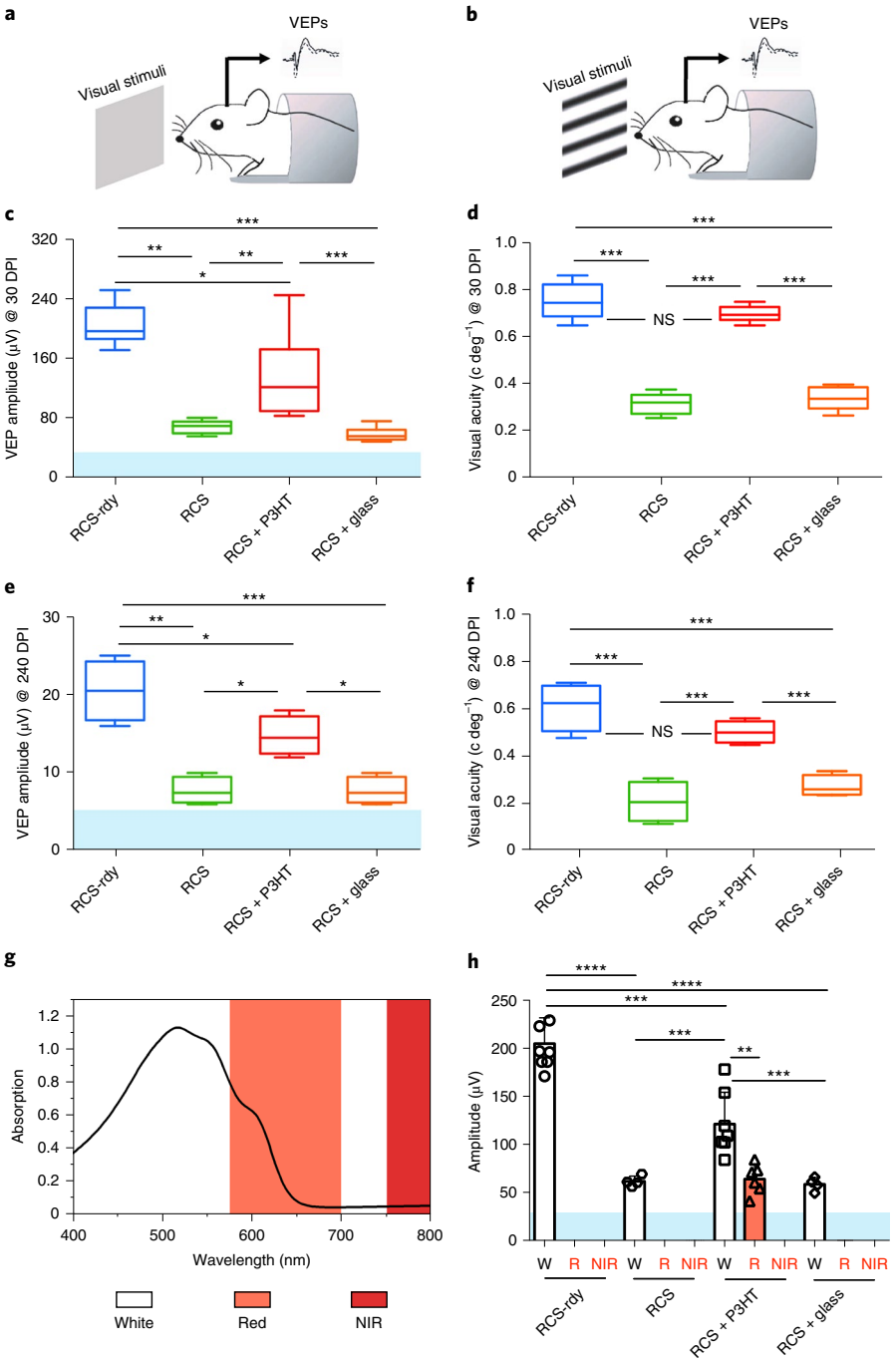

Fig. 5 | Long-term rescue of V1 cortical responses in response to flash and patterned illumination in dystrophic RCS rats injected with P3HT NPs. **a**,**b**, Experimental set-up for VEP recordings in V1 in response to either flash stimuli (**a**; 20 cd m^{-2}; 200 ms, 1 Hz) or horizontal sinusoidal gratings of increasing spatial frequency (**b**; 0.1 to 1 cycle per degree of visual angle) administered at 1 Hz. **c**,**e**, VEP recordings in V1 in response to flash stimuli show a significant improvement of light sensitivity in RCS rats injected with P3HT NPs at both 30 (**c**) and 240 (**e**) DPI. *P < 0.05, **P < 0.01, ***P < 0.001, one-way ANOVA/Tukey tests. Sample size (experimental animals): RCS-rdy, n = 8 and 4; RCS, n = 7 and 4; RCS + P3HT NPs, n = 12 and 4; RCS + glass NPs, n = 6 and 4 for 30 and 240 DPI, respectively. **d**,**f**, The electrophysiological analysis of VEP recordings in response to horizontal sinusoidal gratings reveals a full recovery of visual acuity (c deg^{-1}, cycles per degree of visual angle) at both 30 (**d**) and 240 (**f**) DPI. ***P < 0.001, NS, P > 0.05; one-way ANOVA/Tukey tests. Sample size (experimental animals): RCS-rdy, n = 10 and 4; RCS, n = 10 and 4; RCS + P3HT NPs, n = 6 and 4; RCS + glass NPs, n = 7 and 4 for 30 and 240 DPI, respectively. Box plots in **c**–**f** represent the median (centre line), 25th–75th percentiles (box) and limit of three times the interquartile range. **g**,**h**, To demonstrate the role of P3HT NPs in the light-evoked VEP responses, a separate cohort of animals at 30 DPI was stimulated with white, red and NIR flash stimuli (20 cd m^{-2}; 200 ms, 1 Hz). **g**, The absorbance spectrum of P3HT NPs shows that P3HT is activated by red stimuli (although to a lesser extent as compared with white light), but not by NIR. **h**, The VEP amplitude evoked by white, red and NIR flash stimuli in the four experimental groups reveals that healthy RCS-rdy and dystrophic RCS rats are blind to red and NIR, and that only the P3HT-NP-injected, and not the sham-injected, group displays a significant VEP response to red, but not to NIR stimuli. Data are mean ± s.e.m. with superimposed individual experimental points. **P < 0.01, ***P < 0.001, ****P < 0.0001, one-way ANOVA/Tukey tests. Sample size (experimental animals): RCS-rdy, n = 8; RCS, n = 4; RCS + P3HT NPs, n = 7; RCS + glass NPs, n = 4. In all VEP amplitude plots (**c**,**e**,**h**) the average 2-s.d. noise band has been reported over the baseline (blue area). For exact P values, see Supplementary Table 3.

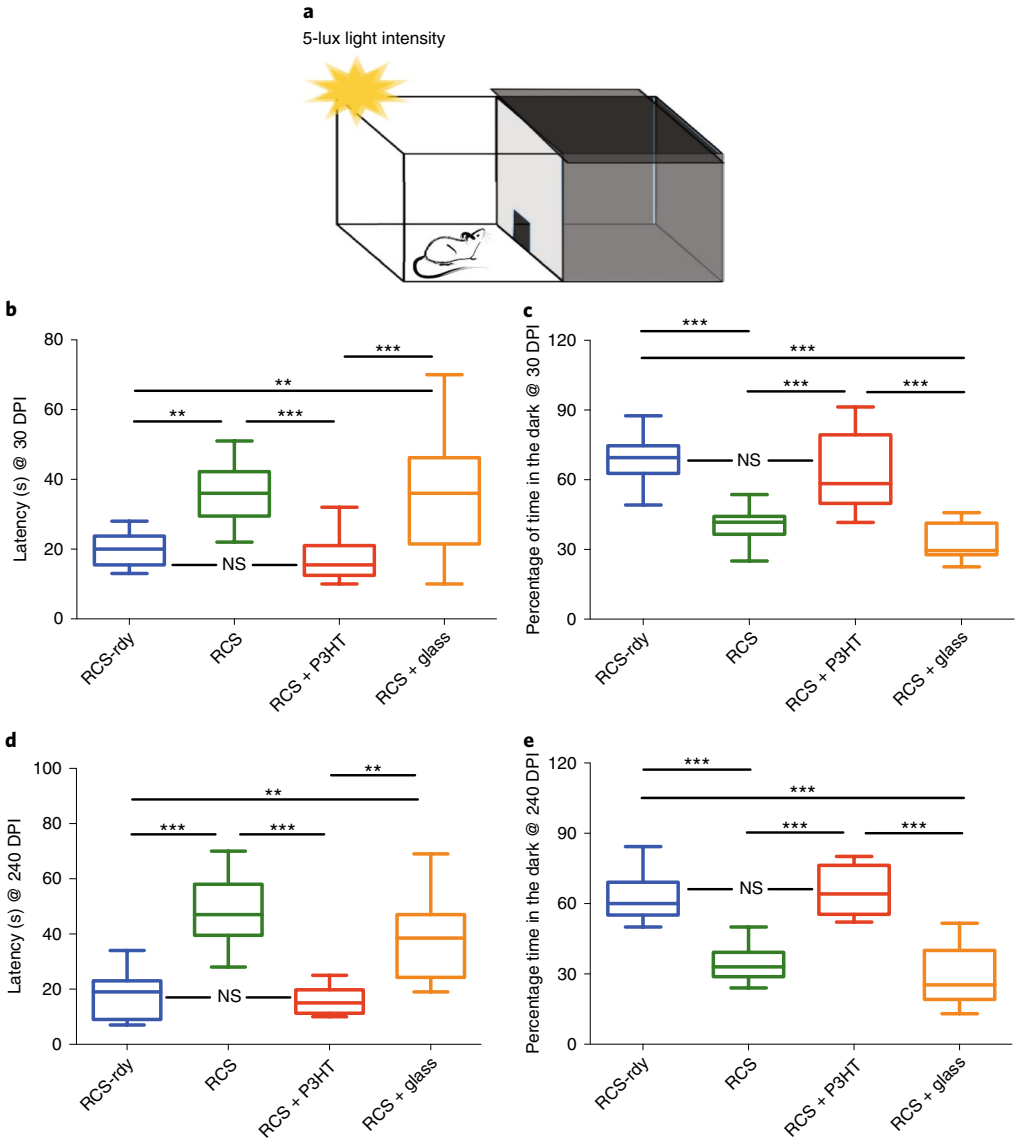

Fig. 6 | Long-term rescue of visually evoked behaviour in dystrophic RCS rats injected with P3HT NPs. a, The light–dark box test revealed the reinstatement of light sensitivity in RCS rats injected with P3HT NPs. **b**–**e**, The behavioural performance was evaluated on the basis of the escape latency from the light compartment (**b**,**d**) and the overall time spent in the dark compartment (**c**,**e**) at both 30 (**b**,**c**) and 240 (**d**,**e**) DPI. $^{**}P < 0.01$, $^{***}P < 0.001$, NS, $P > 0.05$; one-way ANOVA/Tukey tests. Box plots in **b**–**e** represent the median (centre line), 25th–75th percentiles (box) and limit of three times the interquartile range. Sample size (experimental animals): RCS-rdy, $n = 12$ and 7; RCS, $n = 10$ and 9; RCS + P3HT NPs, $n = 24$ and 8; RCS + glass NPs, $n = 10$ and 8 for 30 and 240 DPI, respectively. For exact P values, see Supplementary Table 3.

collectively labelled with recoverin antibodies. Both rod and cone cell bodies were markedly decreased with respect to healthy (RCS-rdy) retinas at 30 DPI and even more at 240 DPI, irrespective of whether RCS rats were non-injected or injected with either P3HT or glass NPs (Fig. 3). In the case of recoverin staining, also labelling a sub-population of bipolar cells, degeneration in all experimental groups of dystrophic RCS rats specifically hit the photoreceptor population, leaving bipolar cells relatively unaffected with respect to RCS-rdy rats (Extended Data Fig. 3). We confirmed these observations by quantitative PCR with reverse transcription (qRT–PCR) analysis of retinal messenger RNA levels of rhodopsin and both short- and long-wave opsin1, which are specifically transcribed by intact and viable rods and cones. All dystrophic RCS animals, irrespective of whether they were non-implanted, implanted with P3HT NPs or sham-implanted with glass NPs, displayed photoreceptor-specific mRNA levels that were two to three orders of magnitude lower than those of age-matched non-dystrophic animals at both 30 and 240 DPI (Extended Data Fig. 4). These results exclude the presence of trophic effects that might slow down photoreceptor degeneration and bias the subsequent functional rescue tests.

The analysis of the GFAP and Iba-1 immunoreactivities, as markers of astrocyte/Müller cell gliosis and microgliosis, as well as the expression of the retinal trophic factor FGF2, revealed the presence of an inflammatory response due to degeneration in all dystrophic RCS groups at both 30 and 240 DPI. NP microinjection in RCS retinas did not further alter the expression of GFAP, Iba-1 or FGF2, indicating the absence of proinflammatory effects of P3HT NPs (Extended Data Fig. 5). This observation was also confirmed by the minimal (<20%) overlap of P3HT fluorescence with the astrocyte/microglial markers (Supplementary Fig. 8).

P3HT NPs rescue visual responses in dystrophic RCS rats

The pupillary light reflex (PLR) is an autonomic reflex integrated at subcortical level driven by the rod–cone and the melanopsin-expressing RGC systems[41]. We evaluated the extent of pupillary constriction as an index of light sensitivity (Fig. 4a)[21]. The PLR was markedly depressed in RCS rats at 4 and 11 months of age, as compared with healthy age-matched RCS-rdy controls at all tested irradiation intensities (1–20 lux) (Fig. 4b,c). In contrast, RCS rats injected with P3HT NPs displayed a clear-cut increase in the evoked pupil constriction over the whole range of irradiances at both 30 and 240 DPI with respect to either untreated or sham-injected RCS animals (Fig. 4b,c and Supplementary Videos 1 and 2). Notably, the PLR responses of RCS rats injected with P3HT NPs fully matched those of healthy controls at both 30 and 240 DPI, indicating a persistent restitutio in integrum. Interestingly, the overall PLR performances naturally decreased with age in all experimental groups, except for RCS animals that received P3HT NPs (Fig. 4d).

We next assessed the electrophysiological restoration of normal visual functions at the cortical level. We first measured the amplitude of electrical responses of the V1 cortex to flashes of light using extracellular recordings of VEPs in the binocular area of V1 (Fig. 5a)[21,42]. VEP responses in untreated dystrophic RCS rats were markedly impaired with respect to healthy RCS-rdy controls already at 4 and even more at 11 months of age, becoming closer to the noise band (Fig. 5c,e), as previously reported for the RCS rat strain[43]. A substantial rescue of light sensitivity was observed in RCS rats injected with P3HT NPs at 30 DPI, with amplitudes of the V1 signal approaching the response of healthy RCS-rdy controls (Fig. 5c and Supplementary Fig. 9a). The rescue of VEP responses in P3HT-NP-injected RCS rats after 240 DPI was qualitatively and quantitatively similar to that observed at 30 DPI, indicating the persistence of the effects over time after a single microinjection (Fig. 5e and Supplementary Fig. 9b).

We next evaluated the quality of the recovered sight by examining the spatial resolution (visual acuity) in response to patterned visual stimuli of increasing spatial frequency (Fig. 5b)[21,42]. While untreated RCS rats displayed a marked impairment in visual acuity (Fig. 5d,f and Supplementary Figs. 10 and 11), RCS rats injected with P3HT NPs displayed a full recovery of acuity to the levels of healthy RCS-rdy controls at 30 DPI (Fig. 5d and Supplementary Fig. 11a). The complete rescue of spatial acuity in RCS rats injected with P3HT NPs was also fully preserved at 240 DPI (Fig. 5f and Supplementary Fig. 11b). In spite of the improvement of VEP responses by P3HT NPs, the increased VEP latency of dystrophic RCS rats was not significantly rescued by the treatment (Extended Data Fig. 6a).

To clarify that the visual rescue is not due to residual or 'regenerating' photoreceptors and that P3HT NPs are indeed responsible for the cortical responses, we measured flash-evoked VEP amplitudes in response to (1) white light (as done above), (2) red light, known not to stimulate photoreceptor responses in the healthy rat retina, but still able to partially stimulate P3HT NPs, and (3) near infrared (NIR), which stimulates neither photoreceptors nor P3HT NPs (Fig. 5g). While white light evoked clear-cut VEP responses in healthy RCS-rdy rats and dystrophic animals injected with P3HT NPs, and NIR light did not evoke responses in any of the four experimental groups, red light triggered a VEP response only in RCS rats bearing P3HT NPs (Fig. 5h and Supplementary Fig. 12). Interestingly, the latencies of VEP responses to white and red light were not significantly different, confirming the same underlying mechanism (Extended Data Fig. 6b). These data unequivocally prove that the rescue of visual cortical responses is indeed attributable to P3HT NPs and not to surviving photoreceptors.

To obtain an independent proof of the light-evoked activation of the visual cortex by retinal signals, we evaluated the V1 metabolic activity by positron emission tomography neuroimaging of the glucose analogue ^{18}F-fluoro-deoxyglucose (^{18}F-FDG)[21]. The tracer enters neuronal cells as a function of their glucose consumption, is phosphorylated by hexokinase and accumulates in the cytosol[44], thus providing a three-dimensional (3D) map of the metabolic activity of V1. Standardized uptake values (SUVs) in the V1 region identified by MRI scans were used to estimate the extent of V1 activation in ^{18}F-FDG-injected animals subjected to a 40-min visual stimulation with light flashes (Extended Data Fig. 7a)[45]. Untreated dystrophic RCS animals displayed a lower SUV in V1 with respect to age-matched RCS-rdy controls (Extended Data Fig. 7b). Consistent with the recovery of visual functions assessed by in vivo electrophysiology, P3HT-NP-injected, but not sham-injected, RCS rats showed a significant increase in average SUV at 240 DPI and became indistinguishable from non-injected RCS-rdy controls.

We finally tested whether bilaterally injected P3HT NPs could rescue visually driven behavioural activity in dystrophic RCS animals using the light–dark box test and evaluating the latency of escape from the illuminated area (5 lux) and the percentage of time spent in the dark (Fig. 6a)[21,46]. Untreated RCS rats at both 4 and 11 months of age displayed a significantly longer latency of escape and no preference for the dark compartment with respect to age-matched RCS-rdy controls (Fig. 6b–e). Strikingly, P3HT-NP-injected, but not sham-injected, RCS rats showed a full recovery in both latency of escape and preference for the dark compartment to the levels of RCS-rdy controls at both 30 and 240 DPI (Fig. 6b–e and Supplementary Videos 3 and 4), in the absence of any change in the overall motor activity (Supplementary Fig. 13).

To definitely prove that the visual rescue of P3HT NPs is not attributable to trophic or proinflammatory effects, a subpopulation of rats belonging to the four experimental groups that underwent all individual tests (a total of 21 rats at 30 DPI and 16 at 240 DPI) was subjected to the analysis of the principal morphofunctional retinal components, in which functional performances at 30 and 240 DPI were individually correlated with either photoreceptor survival (Supplementary Fig. 14) or inflammatory/trophic biomarkers (Supplementary Fig. 15). To better understand the effects of the P3HT-NP injection, we first mapped the cross-correlation between these variables and observed a substantial colinearity among many of them (Extended Data Fig. 8). Except for RCS rats injected with P3HT NPs, visual acuity and visually driven behavioural responses were strongly correlated with photoreceptor cell counts and inversely correlated with inflammatory markers. We then decided to decompose all values into three integrated variables indicating visual responses, inflammatory responses and residual photoreceptor counts at 30 and 240 DPI (Extended Data Fig. 9). In both time windows, data clusters were well separated, with healthy RCS-rdy rats showing the highest visual responses and photoreceptor counts, and the lowest score for inflammatory markers. Both sham-injected and P3HT-NP-injected RCS rats showed no recovery in the photoreceptor cell body numbers ($P > 0.45$) or any worsening of the inflammatory state ($P > 0.55$) with respect to untreated RCS rats. Despite the photoreceptor depletion and the inflammatory state, RCS rats injected with P3HT NPs show unequivocally and significantly stronger visual responses than the untreated or sham-injected animals, fully supporting a direct role of P3HT NPs in visual rescue and ruling out the contribution of trophic effects. No notable correlation of visual performances with the NP layer thickness or the NP/ONL volume ratio was observed, given the highly reproducible distribution of NPs in the outer retina (Supplementary Fig. 16).

P3HT NPs as a liquid retinal prosthesis

Organic semiconductors are carbon-based materials similar to most natural pigments. Among them, conjugated polymers have electron delocalization along their backbone. This bestows optoelectronic

properties typical of semiconductors, while preserving mechanical and processing properties typical of plastics. Akin to biological molecules, conjugated polymers are ideal for interacting with biological tissues, being highly biocompatible, soft and conformable and non-inflammatory[12,13]. Here, we propose a new 'liquid retina device' made of an aqueous suspension of single-component polymeric NPs in the absence of a hole-acceptor layer. Sterile and surfactant-free submicrometre P3HT NPs proved to be effective bioactuators characterized by high surface/volume ratio, large optical absorption cross-section, effective heat dissipation, high biocompatibility due to the intrinsic affinity of their chemical structure with that of biomolecules, and high potential for spatial resolution, with neighbour distances in the range of foveal cones[47].

A recent work[32] shows that water polarization at the polymer surface induces a downshift of the frontier orbital energy, mimicking semiconductor band bending. Upon photoexcitation, negative charge accumulates at the surface, separating from positive charge in the bulk, with oxygen doping reinforcing this effect. Light-evoked depolarization and neuronal firing by P3HT NPs has a capacitive origin and is made possible by the light-dependent charging of the NP surface coupled to a loose-patch conformation of the junctional surface in which the neuronal membrane closely wraps the NPs. With a virtual cleft of <20 nm and cleft resistances above 10–100 MΩ, millivolt depolarizations occur at physiological light intensities. Although the effect has the same size as a postsynaptic potential in central synapses, extensive temporal and spatial summation can occur to reach the firing threshold of the neuron.

These unique features become even more substantial when P3HT NPs are microinjected, with a minimally invasive procedure, into the subretinal space of blind rats, where they fully rescue subcortical, visual responses, visual acuity and metabolic activation of the V1 cortex and light-driven behaviours to the levels of the healthy controls. The retinal responses evoked by P3HT-NP photostimulation in degenerate retinas are characterized by a longer latency than those of healthy retinas, likely due to the extensive rewiring of degenerate retinas[21,30] and to the temporal/spatial summation of photopotentials needed to trigger RGC firing. Notably, P3HT NPs distributed evenly throughout the subretinal space after injection, did not show any tendency to migrate toward the inner retinal layers and maintained the original subretinal distribution over time up to 8 months after injection, ruling out a wide-body diffusion of the injected NPs or their clearance by neurons or glia.

The visual rescue obtained with P3HT NPs is not due to an increased survival of residual photoreceptors, but to a direct effect of the polymeric interface. In fact, (1) NP-injected pink-eyed RCS rats display an extremely severe photoreceptor degeneration with no signs of photoreceptor regeneration following surgery in NP injection; (2) sham-operated RCS rats do not experience any detectable improvement in visual function and their performance fully overlaps with that of untreated RCS rats; (3) visual stimulation with red light, to which healthy rat photoreceptors are blind, elicits visual cortical signals only in RCS rats injected with P3HT NPs.

Conclusions

Several NPs have been recently proposed for neuronal photostimulation or for ameliorating degenerative blindness. Rare-earth NPs are effective in preventing or slowing down photoreceptor degeneration induced by excessive free-radical production[48]. Neuron-targeted gold NPs can trigger photothermal neuronal stimulation[49,50]. Infrared-sensitive upconverting NPs exciting optogenetic actuators[26] endow the retina with infrared sensitivity[27]. In this scenario, the conjugated polymer NPs reported in this study represent an attempt to rescue sensitivity and spatial discrimination in degenerate retinas in response to visible light. Although the limited visual acuity of the animal model does not allow us to conclusively demonstrate the spatial resolution potential of P3HT NPs, the grating acuity obtained in the dystrophic RCS rat equals the best that can be achieved by current implants. The simpler surgical operation with respect to the implantation of a retinal prosthesis and the wide retinal coverage, potentially restoring the complete visual field, opens a new avenue in the clinical applications of conjugated polymers in degenerative blindness. The potential for high spatial resolution of P3HT NPs may extend their applicability to earlier stages of RP and atrophic AMD, once their efficacy is demonstrated in high-resolution retinas. Working as non-genetic light actuators for neuronal activation, semiconducting polymer NPs have a high potential for biomedical applications in degenerative retinal diseases and, possibly, in central nervous system diseases.

Online content

Any methods, additional references, Nature Research reporting summaries, source data, extended data, supplementary information, acknowledgements, peer review information; details of author contributions and competing interests; and statements of data and code availability are available at https://doi.org/10.1038/s41565-020-0696-3.

Received: 21 January 2019; Accepted: 20 April 2020;
Published online: 29 June 2020

References

1. Pascolini, D. & Mariotti, S. P. Global estimates of visual impairment: 2010. *Br. J. Ophthalmol.* **9**, 614–618 (2012).
2. Provis, J. M., Penfold, P. L., Cornish, E. E., Sandercoe, T. M. & Madigan, M. C. Anatomy and development of the macula: specialization and the vulnerability to macular degeneration. *Clin. Exp. Optom.* **88**, 269–281 (2005).
3. Ziccardi, L. et al. Gene therapy in retinal dystrophies. *Int. J. Mol. Sci.* **20**, 22 (2019).
4. Maeda, A., Mandai, M. & Takahashi, M. Gene and induced pluripotent stem cell therapy for retinal diseases. *Annu. Rev. Genom. Hum. Genet.* **20**, 201–216 (2019).
5. Simunovic, M. P. et al. Optogenetic approaches to vision restoration. *Exp. Eye Res.* **178**, 15–26 (2019).
6. Scholl, H. P. et al. Emerging therapies for inherited retinal degeneration. *Sci. Transl. Med.* **8**, 368rv6 (2016).
7. Benfenati, F. & Lanzani, G. New technologies for developing second generation retinal prostheses. *Lab Anim.* **47**, 71–75 (2018).
8. Bloch, E., Luo, Y. & da Cruz, L. Advances in retinal prosthesis systems. *Ther. Adv. Ophthalmol.* **11**, 1–19 (2019).
9. Dagnelie, G. et al. Performance of real-world functional vision tasks by blind subjects improves after implantation with the Argus® II retinal prosthesis system. *Clin. Exp. Ophthalmol.* **45**, 152–159 (2017).
10. Stingl, K. *et al.* Artificial vision with wirelessly powered subretinal electronic implant alpha-IMS. *Proc. Biol. Sci.* **280**, 20130077 (2013).
11. Lorach, H. et al. Photovoltaic restoration of sight with high visual acuity. *Nat. Med.* **21**, 476–482 (2015).
12. Manfredi, G., Colombo, E., Barsotti, J., Benfenati, F. & Lanzani, G. Photochemistry of organic retinal prostheses. *Annu. Rev. Phys. Chem.* **70**, 99–121 (2019).
13. Rivnay, J., Wang, H., Fenno, L., Deisseroth, K. & Malliaras, G. G. Next-generation probes, particles, and proteins for neural interfacing. *Sci. Adv.* **3**, e1601649 (2017).
14. Tian, B. et al. Roadmap on semiconductor-cell biointerfaces. *Phys. Biol.* **15**, 031002 (2018).
15. Ghezzi, D. et al. A hybrid bioorganic interface for neuronal photoactivation. *Nat. Commun.* **2**, 166 (2011).
16. Feyen, P. et al. Light-evoked hyperpolarization and silencing of neurons by conjugated polymers. *Sci. Rep.* **6**, 22718 (2016).
17. Ghezzi, D. et al. A polymer optoelectronic interface restores light sensitivity in blind rat retinas. *Nat. Photonics* **7**, 400–406 (2013).
18. Gautam, V., Rand, D., Hanein, Y. & Narayan, K. S. A polymer optoelectronic interface provides visual cues to a blind retina. *Adv. Mater.* **26**, 1751–1756 (2014).
19. Gal, A. et al. Mutations in MERTK, the human orthologue of the RCS rat retinal dystrophy gene, cause retinitis pigmentosa. *Nat. Genet.* **26**, 270–271 (2000).
20. Antognazza, M. R. et al. Characterization of a polymer-based fully organic prosthesis for implantation into the subretinal space of the rat. *Adv. Healthc. Mater.* **5**, 2271–2282 (2016).

21. Maya-Vetencourt, J. F. et al. A fully organic retinal prosthesis restores vision in a rat model of degenerative blindness. *Nat. Mater.* **16**, 681–689 (2017).
22. Rossi, E. A. & Roorda, A. The relationship between visual resolution and cone spacing in the human fovea. *Nat. Neurosci.* **13**, 156–157 (2010).
23. Di Maria, F., Lodola, F., Zucchetti, E., Benfenati, F. & Lanzani, G. The evolution of artificial light actuators in living systems: from planar to nanostructured interfaces. *Chem. Soc. Rev.* **47**, 4757–4780 (2018).
24. Feng, L. et al. Conjugated polymer nanoparticles: preparation, properties, functionalization and biological applications. *Chem. Soc. Rev.* **42**, 6620–6633 (2013).
25. Colombo, E., Feyen, P., Antognazza, M. R., Lanzani, G. & Benfenati, F. Nanoparticles: a challenging vehicle for neural stimulation. *Front. Neurosci.* **10**, 105 (2016).
26. Chen, S. et al. Near-infrared deep brain stimulation via upconversion nanoparticle-mediated optogenetics. *Science* **359**, 679–684 (2018).
27. Ma, Y. et al. Mammalian near-infrared image vision through injectable and self-powered retinal nanoantennae. *Cell* **177**, 243–255 (2019).
28. Tuncel, D. & Demir, H. V. Conjugated polymer nanoparticles. *Nanoscale* **2**, 484–494 (2010).
29. Zangoli, M. et al. Engineering thiophene-based nanoparticles to induce phototransduction in live cells under illumination. *Nanoscale* **9**, 9202–9209 (2017).
30. Pu, M., Xu, L. & Zhang, H. Visual response properties of retinal ganglion cells in the Royal College of Surgeons dystrophic rat. *Invest. Ophthalmol. Vis. Sci.* **47**, 3579–3585 (2006).
31. Martino, N. et al. Photothermal cellular stimulation in functional bio-polymer interfaces. *Sci. Rep.* **5**, 8911 (2015).
32. Mosconi, E. et al. Surface polarization drives photo-induced charge separation at the P3HT/water interface. *ACS Energy Lett.* **1**, 454–463 (2016).
33. Fendyur, A., Mazurski, N., Shappir, J. & Spira, M. E. Formation of essential ultrastructural interface between cultured hippocampal cells and gold mushroom-shaped MEA—toward "IN-CELL" recordings from vertebrate neurons. *Front. Neuroeng.* **4**, 14 (2011).
34. Shmoel, N. et al. Multisite electrophysiological recordings by self-assembled loose-patch-like junctions between cultured hippocampal neurons and mushroom-shaped microelectrodes. *Sci. Rep.* **6**, 27110 (2016).
35. Hanson, L., Lin, Z. C., Xie, C., Cui, Y. & Cui, B. Characterization of the cell-nanopillar interface by transmission electron microscopy. *Nano Lett.* **12**, 5815–5820 (2012).
36. Pardue, M. T. et al. Neuroprotective effect of subretinal implants in the RCS rat. *Invest. Ophthalmol. Vis. Sci.* **46**, 674–682 (2005).
37. Morimoto, T. et al. Transcorneal electrical stimulation promotes the survival of photoreceptors and preserves retinal function in Royal College of Surgeons rats. *Invest. Ophthalmol. Vis. Sci.* **48**, 4725–4732 (2007).
38. Zhou, W. T. et al. Electrical stimulation ameliorates light-induced photoreceptor degeneration *in vitro* via suppressing the proinflammatory effect of microglia and enhancing the neurotrophic potential of Müller cells. *Exp. Neurol.* **238**, 192–208 (2012).
39. Lorach, H. et al. Long-term rescue of photoreceptors in a rodent model of Retinitis Pigmentosa associated with MERTK mutation. *Sci. Rep.* **8**, 11312 (2018).
40. LaVail, M. M. & Battelle, B. A. Influence of eye pigmentation and light deprivation on inherited retinal dystrophy in the rat. *Exp. Eye Res.* **21**, 167–192 (1975).
41. Lucas, R. J. et al. Diminished pupillary light reflex at high irradiances in melanopsin-knockout mice. *Science* **299**, 245–247 (2003).
42. Maya Vetencourt, J. F. et al. The antidepressant fluoxetine restores plasticity in the adult visual cortex. *Science* **320**, 385–388 (2008).
43. McGill, T. J., Douglas, R. M., Lund, R. D. & Prusky, G. T. Quantification of spatial vision in the Royal College of Surgeons rat. *Invest. Ophthalmol. Vis. Sci.* **45**, 932–936 (2004).
44. Phelps, M. E. Positron computed tomography studies of cerebral glucose metabolism in man: theory and application in nuclear medicine. *Semin. Nucl. Med.* **11**, 32–49 (1981).
45. Hustinx, R., Smith, R. J., Benard, F., Bhatnagar, A. & Alavi, A. Can the standardized uptake value characterize primary brain tumors on FDG-PET? *Eur. J. Nucl. Med.* **26**, 1501–1509 (1999).
46. Bourin, M. & Hascoet, M. The mouse light/dark box test. *Eur. J. Pharm.* **463**, 55–65 (2003).
47. Smith, G. & Atchinson, D.A. in *The Eye and Visual Optical Instruments* pp 291–316 (Cambridge University Press, 1997).
48. Chen, J., Patil, S., Seal, S. & McGinnis, J. F. Rare earth nanoparticles prevent retinal degeneration induced by intracellular peroxides. *Nat. Nanotechnol.* **1**, 142–150 (2006).
49. Shapiro, M. G., Homma, K., Villarreal, S., Richter, C. P. & Bezanilla, F. Infrared light excites cells by changing their electrical capacitance. *Nat. Commun.* **3**, 736 (2012).
50. Carvalho-de-Souza, J. L. et al. Photosensitivity of neurons enabled by cell-targeted gold nanoparticles. *Neuron* **86**, 207–217 (2015).

Methods

Production and characterization of P3HT NPs. P3HT was synthesized by oxidative polymerization of 3-hexyl-thiophene (1 g in 40 ml of $CHCl_3$) with ferric chloride according to a known procedure[51]. The method displayed high reproducibility in the characteristics of the polymer, such as regioregularity (as estimated from ^{1}H-NMR), dispersity and spectroscopic features. The P3HT NPs were then obtained from freshly prepared P3HT solution in common organic solvents using the reprecipitation technique in the absence of surfactants, as previously described[51,52]. Briefly, P3HT (8 mg) dissolved in 300 µl of tetrahydrofuran was added dropwise via a Hamilton syringe to 4 ml of sterilized Milli-Q water under magnetic stirring. The obtained suspension was subjected to dialysis (12,000-g-mol^{-1} cutoff) against 2 l of sterile Milli-Q water for 2 d to remove the residual organic solvent. Differential centrifugation was used to separate P3HT NPs into fractions of different sizes[29]. The dispersed fraction was collected for biological use and further characterized. The whole process was carried out under sterile conditions. As a control, non-fluorescent and fluorescent glass (SiO_2) NPs of comparable size were obtained from Microparticles GmbH and Micromod Partikeltechnologie GmbH respectively (SiO_2-R-L3235, 259-nm nominal diameter, and sicastar-redF, excitation 569 nm, emission 585 nm, 300-nm nominal diameter) and autoclave sterilized. Glass and P3HT NPs were characterized by SEM and DLS. Briefly, for SEM imaging, a drop of NP solution was deposited on a glass coverslip; coverslips were then sputter-coated with a 10-nm layer of gold in an Ar-filled chamber (Cressington, 208HR sputter coater) and imaged using a JEOL JSM-6490LA scanning electron microscope. NPs were characterized by size in distilled water by the DLS technique using a Malvern Zetasizer NanoZS (Malvern Panalytical). Glass and P3HT NPs were sonicated for 1 min using a Branson 2510 bath sonicator (Branson Ultrasonic). The size of NPs dispersed in deionized water was determined at a concentration of 1 mg ml^{-1}. Measurements were conducted at 25 °C by transferring 1 ml of stock solution to a square disposable cuvette for DLS analysis. A 50-mW laser at 638 nm wavelength was used as the light source. For each sample, measurements were recorded at 173° (backscatter) detection angle and performed in triplicate, each counting at least 10 runs.

Experimental animals and ethical approval. All animal manipulations and procedures were performed in accordance with the guidelines established by the European Community Council (Directive 2012/63/EU of 22 September 2010) and were approved by the Italian Ministry of Health (authorization no. 645/2015-PR). Inbred RCS pink-eyed dystrophic animals, together with congenic non-dystrophic (RCS-rdy) controls, were provided by M. M. La Vail (Beckman Vision Centre, University of California San Francisco)[40]. Rat colonies were bred under standard conditions with ad libitum access to food and water under a 12/12-h light/dark cycle.

Patch-clamp recordings on RGCs. Dystrophic retinas were dissected from the enucleated eyes of 12–14-month-old RCS rats. Eyes were enucleated in dim red light and kept in carbo-oxygenated Ames medium (Sigma-Aldrich). The cornea, iris, lens and vitreous were removed but left in contact with the sclera. Each retina was subdivided into two pieces that were transferred to the microscope stage, continuously perfused with carbo-oxygenated Ames medium. We puffed RGCs with 1-mg-ml^{-1} P3HT NPs using borosilicate pipettes (1–2 MΩ). For further details, see Supplementary Information.

MEA recordings on retina explants. Dystrophic retinas were dissected from the enucleated eyes of 12–14-month-old RCS rats as described above. Retinas from 12-month-old congenic non-dystrophic RCS-rdy rats were also employed. Each piece of retina was placed, RGC-side down after a subretinal injection of NPs, onto a 60-electrode MEA chip using the MEA1060-inv system (Multi Channel Systems). To investigate the involvement of TRPV and ASIC channels in the mechanism of phototransduction, ruthenium red (10 µM; Sigma-Aldrich) and amiloride (100 µM; Tocris) were respectively added to the recording medium. Light-evoked extracellular activity in MEA experiments was obtained with a fibre-coupled Lumencor light-emitting diode system (Spectra X) peaking at 530 nm, fed to an inverted Nikon Eclipse Ti microscope. The illumination spot covered an area of about 1 mm^2 with a power density ranging from 1 to 40 mW mm^{-2}. Data were acquired at 25 kHz and filtered between 200 Hz and 3 kHz. Spike detection and sorting were performed using MC Rack software (version 4.6.2; Multi Channel Systems). Light-evoked firing activity was assessed by selecting those RGCs displaying a statistically significant modulation of firing that was time-locked to the light stimulus with respect to the baseline (spontaneous activity). The response latency was defined as the time needed to reach the peak firing rate starting from the onset of the light stimulus.

Cell fixation and SEM/FIB imaging. Primary cortical neurons prepared from E18 Sprague Dawley rat embryos and grown on glass coverslips drop-cast with P3HT NPs were fixed at 14 days in vitro with a 2.5% solution of glutaraldehyde in sodium cacodylate buffer (0.1 M) for 60 min at room temperature. Staining in a 20-mM glycine solution in buffer was performed to reduce the signal-to-noise ratio for subsequent imaging. Then, a reduced osmium–thiocarbohydrazide–osmium (RO–T–O) staining protocol was performed, followed by 1 h negative staining with 5% uranyl acetate in aqueous solution in darkness at 4 °C. A final staining of the cytoskeleton was performed in tannic acid (3 min) before embedding the samples in a thin layer of Epon resin[53]. The excess resin was removed by washing the samples in ethanol before overnight polymerization at 65 °C. After polymerization, a thin gold layer (8 nm) was deposited on the samples by plasma sputtering. Cross-sectional imaging of the fixed neurons was obtained with a dual-beam Helios Nanolab 650 (Thermo Fisher), which provides an electron beam (SEM), an ion beam (FIB) and a gas injection system. After coating the neuron with a thin (~0.5-µm) platinum layer via the gas injection system, the neuron was cut with the FIB with an ionic current of 9.3 nA to reveal the cell–NP interface. Finally, a polishing ionic current of 0.79 nA was exploited to allow a clear imaging of the cell interior. The ion acceleration voltage was 30 kV for all FIB processes. The neuron–NP interface was imaged by SEM at a 52° tilt angle (3 kV, 0.20–0.40 nA). Backscattered electrons were collected using a through-lens detector in immersion mode for improved resolution. The colours of the SEM images have been inverted to highlight the cellular components.

Table 1 | Primary antibody dilutions for the immunolabeling of retinal sections

Primary antibody	Supplier	Species	Type	Dilution
Anti-rhodopsin	Invitrogen	Mouse	Monoclonal	1:100
Anti-cone arrestin	Merck Millipore	Rabbit	Polyclonal	1:250
Anti-recoverin	Merck Millipore	Rabbit	Polyclonal	1:1,000
Anti-GFAP	Sigma-Aldrich	Mouse	Monoclonal	1:200
Anti-iba1	Thermo Fischer	Goat	Polyclonal	1:500
Anti-FGF2	Merck Millipore	Mouse	Monoclonal	1:150

Retina immunohistochemistry. Experimental animals were euthanized by CO_2 inhalation followed by cervical dislocation. Eyes were enucleated keeping track of the eye orientation during the staining process. Eyes were fixed in 4% paraformaldehyde in 0.1-M PBS for 6 h, extensively washed in 0.1-M PBS, and cryoprotected by equilibration with 30% sucrose. Eyecups were obtained by removing the cornea, the iris and the lens and then embedded in optimal cutting temperature mounting medium (Tissue-Tek; QIAGEN), frozen overnight at −20 °C and cryosectioned at 50 µm using an MC5050 cryostat (Histo-Line Laboratories). Sections were mounted on gelatin-coated glass slides and maintained at −20 °C until processed. We evaluated the size and the distribution of P3HT NPs from bisbenzimide-stained sections (1:300, Hoechst; 1 min at room temperature) by acquiring the endogenous P3HT fluorescence (λ_{ex}, 514 nm; λ_{em}, 600–650 nm) with a Leica SP8 confocal microscope. For all the morphological analyses, we used the following protocol: sections were first incubated with 10% fetal bovine serum (Gibco) at room temperature for 1 h to block non-specific antibody binding and then incubated overnight at 4 °C with the primary antibody of interest or with isolectin GS-IB4 from *Griffonia simplicifolia* Alexa Fluor 488 conjugate (1:10,000, Invitrogen) at the dilutions reported in Table 1. Alexa Fluor 488- or 637-conjugated; secondary antibodies were diluted 1:300 and incubated at room temperature for 4 h. Retinal sections were imaged with a Leica SP8 confocal microscope.

Analysis of the NP distribution. The cluster volumes and centroids of P3HT/glass NPs were evaluated in 456 × 456 × 50 µm^3 using ImageJ (NIH) with an *XY* resolution of 2,048 × 2,048 pixels and *Z* steps of about 6 µm (3D Object Counter Plugin), then imported into MATLAB (MathWorks) for density, distribution and centre-to-centre calculations using custom-written scripts. Cluster density was estimated in each *z*-stack volume by calculating centroid centre-to-centre distances between clusters using the following equation:

$$D_{ij} = \sqrt{(x_i - x_j)^2 + (y_i - y_j)^2 + (z_i - z_j)^2} - (r_i + r_j)$$

where D_{ij} represents the distance between clusters *i* and *j*, *x*/*y*/*z* represent the Cartesian coordinates for each cluster and *r* represents the average radius of each cluster. This was repeated for the number of pairs (*P*) of clusters for *N* clusters in each *z*-stack,

$$P = \frac{N \times (N-1)}{2}$$

The minimum D_{ij} was averaged for each number of retinas (*N*), using the following equation:

$$\sum_{1 \le i < j \le N}^{N} \frac{D_{ij}}{P}$$

before averaging all values over each condition for statistical analysis. For further details, see Supplementary Information.

Pupillary light reflex. Following dark adaptation for at least 1 h and a light isoflurane anaesthesia, rats were positioned with the eye to be recorded perpendicular to an infrared-sensitive camera fitted with a Leica macro lens. Animals were subjected to a 2-s dim green light exposure of increasing irradiance provided by a light-emitting diode source (515 nm) through the same optical path administered at 10-min intervals. Sequential images were captured with a Hamamatsu camera at a 5-Hz frame rate. Background illumination was provided by an infrared light-emitting diode source (850 nm) throughout the experiment. Pupil area was determined offline from individual video frames before and after light exposure. To facilitate comparisons, pupil areas (a_i) were expressed relative to the dilated area immediately before each exposure (a_0). The effective intensity of each exposure was measured with a lux meter.

In vivo electrophysiology. Animals were anaesthetized with isofluorane (3% induction; 2% maintenance in oxygen) and placed in a stereotaxic frame. Anaesthesia level was stable throughout the experiment and electrocardiogram and body temperature (37 °C) were continuously monitored. A hole was drilled in the skull, corresponding to the binocular portion of V1 (Oc1B). After exposure of the brain surface, the dura mater was gently removed, and a micropipette (2 MΩ) filled with NaCl (3 M) was inserted into the cortex 5 mm from λ (intersection between the sagittal and the lambdoid sutures). Both eyes were fixed and kept wet and open throughout the analysis by means of adjustable metal rings. Light sensitivity and visual acuity were measured using VEPs[21,42,54,55]. During recording through one eye, the other was covered by a black adhesive tape. To prevent sampling bias, VEPs were recorded at three distinct penetrations within Oc1b, at 100- and 400-μm depths for each penetration. Signals (average of 50 sweeps) were amplified, band-pass filtered (0.1–100 Hz) and analysed, as described previously[56]. In the case of light sensitivity, visual stimuli were flashes of the same luminance (20 cd m^{-2}, 200 ms, 1 Hz; Fig. 5a) of white light (400–700 nm), red light (575–700 nm) or infrared light (750–800 nm). In the case of spatial acuity, visual stimuli were horizontal sinusoidal contrast-reversing gratings of increasing spatial frequencies (0.1 to 1 cycle per degree of visual angle) at 1 Hz (Fig. 5b). All visual stimuli were generated by a VSG2/2 card running custom software, displayed on a monitor (20-×-22-cm^2 area; 100% of contrast) positioned 20 cm from the rat's eyes and centred on the previously determined receptive fields. While light sensitivity to the various wavelengths was evaluated on the basis of the amplitude of the VEP response to light flashes, visual acuity was obtained using white light by extrapolation to zero amplitude of the linear regression through the last four or five data points of VEP amplitude versus the logarithm of spatial frequency[54–56]. To rule out equipment-related electrical artefacts, at the end of each session, a 'control' electrophysiological recording was performed covering the animal's eyes with black adhesive. As for detection of VEPs, a deflection of the basal electrical signal in Oc1b was considered physiologically relevant when it was more than twice the s.d. of the noise[57,58]. Care was taken that the recorded signals were at comparable eccentricities in the various experimental groups. Using homemade software (1ChVEPs), the following parameters were computed: (1) the amplitude of the signal, taken as the peak-to-baseline distance, and (2) the latency of the signal, computed as the distance between the initiation of the light stimulus and the signal peak.

Light–dark box test. The light–dark test, based on the innate aversion of nocturnal rodents to brightly illuminated areas[21,46], was used as an index of light sensitivity. The trials were performed in a two-compartment box consisting of a 'light' compartment and a 'dark' compartment communicating through a small door located in a dark experimental room. After dark adaptation for 30 min, the animal is introduced into the "light" compartment, which is illuminated with a 5-lux intensity. Six-minute video recordings were performed to monitor the latency of escape from the illuminated area and the percentage of time spent in each compartment. The number of transitions between the two compartments was also monitored as an index of light-independent motor activity.

Statistics and reproducibility. Data are expressed as box plots or means ± s.e.m. (in the case of normal distribution), with n as the number of independent animals or independent preparations in in vitro/ex vivo studies. Estimates of effect sizes were obtained using the formula

$$n = Z^2 \times \sigma^2 / \Delta^2$$

where Z is the value of the distribution function $f(\alpha, \beta)$ (with α and β type-I and type-II errors, respectively), σ is the s.d. of the groups and Δ is the minimum percentage difference thought to be biologically relevant[59], and setting $Z = 1.96$ (for $\alpha = 0.05$ and $1 - \beta = 0.9$), $\Delta = 0.2$ (20%) and $\sigma = 0.2–03$ on the basis of similar experiments and our preliminary data. The box-plot elements are the following: centre line, median (Q2); square symbol, mean; box limits, 25th (Q1)–75th (Q3) percentiles; whisker length, determined by the outermost data points within three times the interquartile range (Q3 − Q1). Normal distribution was assessed using the D'Agostino–Pearson normality test. To compare two sample groups, either the Student t-test or the Mann–Whitney U-test was used. To compare more than two normally distributed sample groups, one- or two-way ANOVA followed by post hoc multiple comparison tests was used. $P < 0.05$ was considered significant. Statistical analysis was carried out using OriginPro-9 (OriginLab) and Prism v6.07 (GraphPad Software). The component analysis was performed using Python 3 and the scikit-learn package[60]. Correlation maps were plotted using the Python 3 seaborn package (https://doi.org/10.5281/zenodo.1313201). The three summarizing variables used for 3D analysis were obtained by normalization of the starting variables to the average of the healthy RCS-rdy group and pooling under the following three components: visual response = PLR + VEPs + acuity + dark persistence; inflammatory state = GFAP + IBA-1 + FGF2; surviving photoreceptors = rhodopsin + cone arrestin + ONL density. The equality hypothesis among groups was conducted using a permutation test with 5% alpha level[61]. Group analysis on data was conducted using a naive Bayes classifier with diagonal sigma matrices, and data were plotted in a 3D space using Python 3 matplotlib library[62].For further details, see Supplementary Information.

For further details of fabrication of planar P3HT/PET devices, studies in HEK293 cells, studies in primary neurons, surgical injection procedures, in vivo imaging of the retinal implant, RNA preparation and real-time PCR analysis, and positron emission tomography imaging, see Supplementary Information.

Reporting Summary. Further information on research design is available in the Nature Research Reporting Summary linked to this article.

Data availability

The data that support the plots within this paper together with other findings of this study are available from the corresponding author upon reasonable request.

Code availability

Custom codes and software used in this paper can be obtained from the corresponding authors on request.

References

51. Barbarella, G., Bongini, A. & Zambianchi, M. Regiochemistry and conformation of poly(3-hexylthiophene) via the synthesis and the spectroscopic characterization of the model configurational triads. *Macromolecules* **27**, 3039–3045 (1994).
52. Shimizu, H., Yamada, M., Wada, R. & Okabe, M. Preparation and characterization of water self-dispersible poly(3-hexylthiophene) particles. *Polym. J.* **40**, 33–36 (2007).
53. Santoro, F. et al. Revealing the cell-material interface with nanometer resolution by focused ion beam/scanning electron microscopy. *ACS Nano* **11**, 8320–8328 (2017).
54. Pizzorusso, T. et al. Structural and functional recovery from early monocular deprivation in adult rats. *Proc. Natl Acad. Sci. U. S. A.* **103**, 8517–8522 (2006).
55. Maya-Vetencourt, J. F. et al. Experience-dependent expression of NPAS4 regulates plasticity in adult visual cortex. *J. Physiol.* **590**, 4777–4787 (2012).
56. Huang, Z. J. et al. BDNF regulates the maturation of inhibition and the critical period of plasticity in mouse visual cortex. *Cell* **98**, 739–755 (1999).
57. Porciatti, V., Pizzorusso, T. & Maffei, L. The visual physiology of the wild type mouse determined with pattern VEPs. *Vis. Res.* **39**, 3071–3081 (1999).
58. Porciatti, V., Pizzorusso, T. & Maffei, L. Electrophysiology of the postreceptoral visual pathway in mice. *Doc. Ophthalmol.* **104**, 69–82 (2002).
59. Krzywinski, M. & Altman, N. Power and sample size. *Nat. Methods* **10**, 1139–1140 (2013).
60. Pedregosa, F. et al. Scikit-learn: machine learning in Python. *J. Mach. Learn. Res.* **12**, 2825–2830 (2011).
61. Pitman, E. J. G. Significance tests which may be applied to samples from any populations. *J. R. Stat. Soc.* **4**(Suppl.), 119 (1937).
62. Hunter, J. D. Matplotlib: a 2D graphics environment. *Comput. Sci. Eng.* **9**, 90–95 (2007).

Acknowledgements

We thank M. M. La Vail (Beckman Vision Centre, University of California San Francisco) for providing non-dystrophic RCS-rdy+ and dystrophic RCS rats, N. De Petrocellis and N. Forte (CNR Institute for Biomolecular Chemistry) for stably hTRPV1-transfected HEK293 clones, E. Lingueglia (CNRS Institute of Molecular and Cellular Pharmacology) for providing the complementary DNA for the ASIC1a channel, A. Desii, S. Francia and M. Salerno (Istituto Italiano di Tecnologia) for help in the preparation and characterization of NPs, M. Cilli and A. Buschiazzo (IRCCS Ospedale Policlinico San Martino) for assistance in the surgical procedures and help in positron emission tomography imaging and R. Ciancio, I. Dallorto, A. Mehilli, R. Navone and D. Moruzzo (Istituto Italiano di Tecnologia for technical assistance. The work was supported by the Italian Ministry of Health (project RF-2013-02358313 to G.P., G.L. and F.B.), Fondazione Cariplo (project 2018-0505 to G.L., F.B. and G.P.), Compagnia di San Paolo (project 9798 to J.F.M.-V.), H2020-MSCA-ITN 2019 "Entrain Vision" (project 861423 to F.B.) and EuroNanoMed3 (project 2019-132 "NanoLight" to F.B.). The support of the Ra.Mo. Foundation, Rare Partners srl and Fondazione 13 Marzo is also acknowledged.

Author contributions

J.F.M.-V. followed all in vivo experiments by performing electrophysiology and behavioural analyses under the supervision of F.B. and assisted in the optical coherence tomography and positron emission tomography trials; G.P., M.M. and A. Russo developed and executed the subretinal microinjection; M.M. performed optical coherence tomography analysis; G. Manfredi, J.B. and F.D.M. fabricated the NPs and characterized them under the supervision of G.L.; E.C., S.D.M., M.L.D., E.D.P., M.D. and M.B. performed the in vitro/ex vivo electrophysiological and EM experiments on HEK cells, neurons and retinal explants under the supervision of F.B.; V.C., F.T., L.E., D.S. and C.M. executed positron emission tomography experiments under the supervision of G.S.; D.S., G. Mantero and C.E. performed histological analyses under the supervision of S.D.M. and J.F.M.-V.; A. Rocchi performed the qRT–PCR experiments; J.F.M.-V., G.L. and F.B. wrote the manuscript; F.P. revised the manuscript; F.B., G.P., J.F.M.-V. and G.L. conceived, supervised and financed the project. All authors discussed the experimental results and commented on the manuscript.

Competing interests

The P3HT NPs studied in this paper are the subject of the US patent application US 16/005248 'Eye-injectable polymeric nanoparticles and method of use therefor' by Istituto Italiano di Tecnologia and Ospedale Sacrocuore Don Calabria, with J.F.M.-V., M.M., G.P., F.B. and G.L. as inventors. The other authors declare no competing interests.

Additional information

Supplementary information is available for this paper at https://doi.org/10.1038/s41565-020-0696-3.

Correspondence and requests for materials should be addressed to G.L. or F.B.

Reprints and permissions information is available at www.nature.com/reprints.

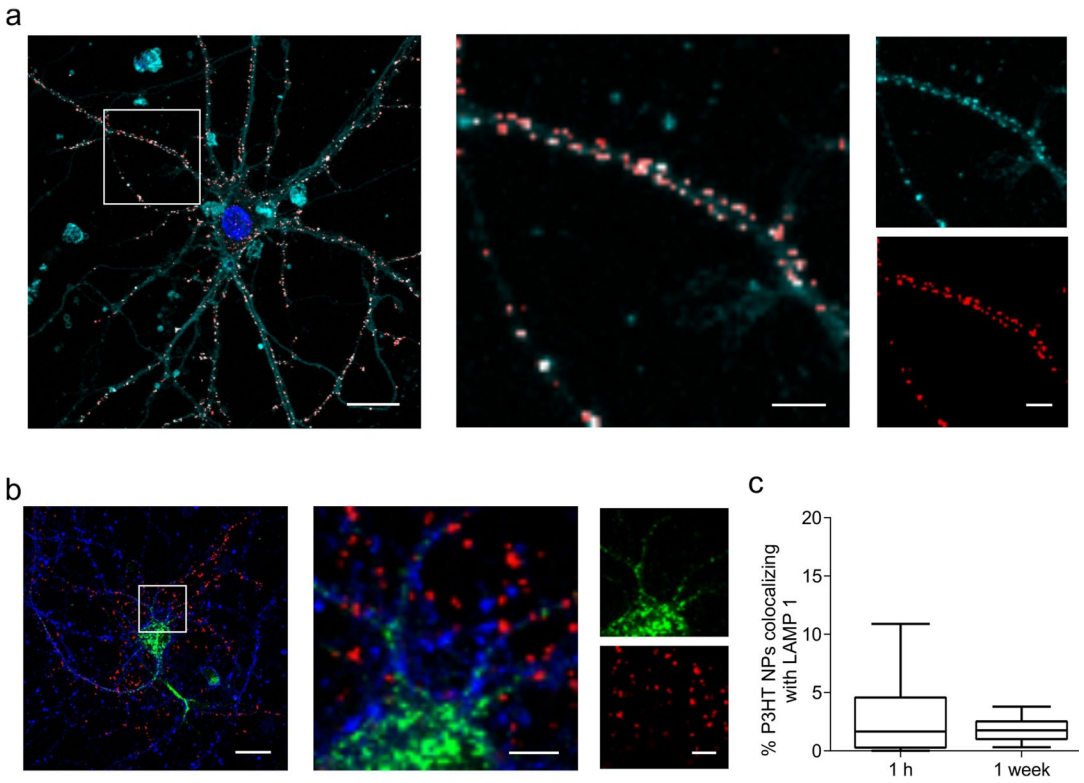

Extended Data Fig. 1 | P3HT nanoparticles incubated with primary neurons are not internalized. a, Primary cortical neurons exposed to P3HT-NPs for 1 h were live stained with Cell Mask and analysed by confocal imaging. Cell Mask (cyan) labels the neuronal membrane, bisbenzimide (blue) highlights cell nuclei and the intrinsic P3HT fluorescence (red) visualizes NPs. In the middle panel, a higher magnification image of the neuron shows the co-localization of P3HT-NPs with the membrane (pink overlaid areas). The results are representative of n = 3 independent neuronal preparations. **b**, To quantify NP internalization, neurons were exposed to P3HT-NPs for either 1 h (shown) or 1 week (not shown) fixed, double immunostained for βIII-tubulin (blue) and the specific lysosomal marker LAMP1 (green) and analysed by confocal microscopy. **c**, Box plot of the extent of NPs/LAMP1 co-localization, quantified by acquiring 3D z-stack confocal images. The median P3HT NPs/LAMP1 volume ratios were 1.65% and 1.75% for 1-h and 1-week incubations, respectively. Box plots represent the median (centre line), mean (square), 25th-75thpercentiles (box) and the limit of 3-fold the interquartile range. Sample size: n = 22 neurons from 2 independent neuronal preparations. Scale bars, 20 μm (main images); 5 μm (zoomed images).

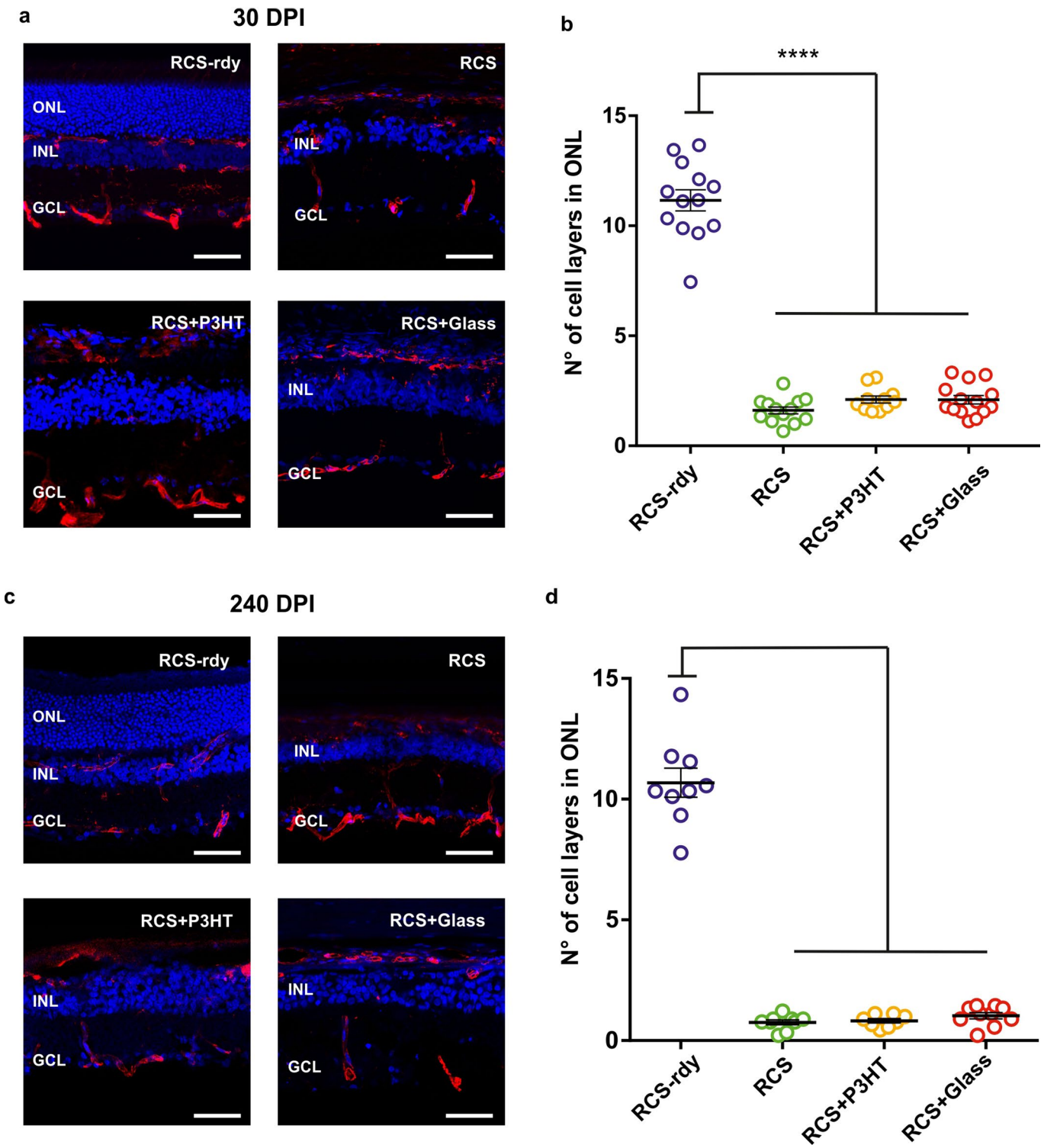

Extended Data Fig. 2 | Quantification of cell bodies in the ONL of dystrophic RCS rats at 30 and 240 DPI. The boundaries of the avascular ONL were determined in transversal sections of representative healthy and dystrophic retinas dissected at 30 DPI (**a**) and 240 DPI (**c**) by histochemistry with isolectin GS-IB4 (red) staining retinal and choroidal vessels, combined with cell nuclear staining with bisbenzimide (blue). A clear-cut thinning of the ONL associated with widening of the INL was present at both 30 DPI and 240 DPI. Quantification of the number of cell layers labelled with bisbenzimide in the ONL revealed a massive decrease of the nuclear rows of photoreceptors in all dystrophic retinas (non-injected, P3HT-NP injected or sham Glass-NP injected) already at 30 DPI (4 months-old rats; **b**), that further progressed at 240 DPI (11 months-old rats; **d**). Means ± sem are shown together with dots representing the mean value obtained for each animal from 9 samplings (3 samples/field and 3 fields/retina). *** $p < 0.001$, one-way ANOVA/Bonferroni's tests. Data are means±sem with superimposed individual experimental points. Sample size (experimental animals) @ 30 DPI: RCS-rdy, n = 13; RCS, n = 13; RCS + P3HT, n = 11; RCS + Glass, n = 14. Sample size (experimental animals) @ 240 DPI: RCS-rdy, n = 9; RCS, n = 9; RCS + P3HT, n = 8; RCS + Glass, n = 10. For exact p values, see Supplementary Table 3. ONL, outer nuclear layer; INL, inner nuclear layer; GCL, ganglion cell layer. Scale bar, 100 µm.

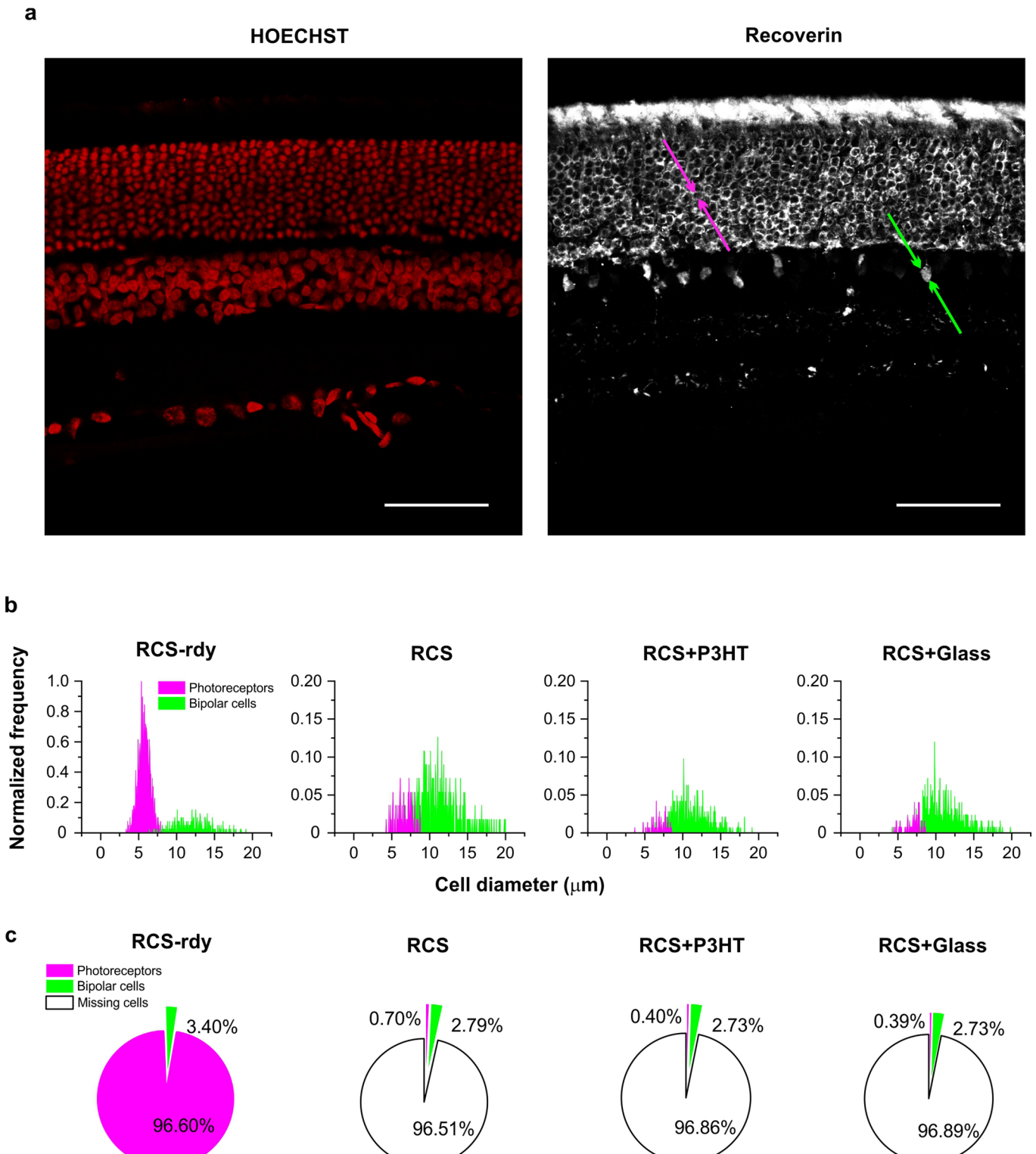

Extended Data Fig. 3 | See next page for caption.

Extended Data Fig. 3 | Degeneration in dystrophic RCS retinas selectively hits recoverin-positive photoreceptors in the ONL. a, Representative image of a retina section from n = 5 non-dystrophic RCS-rdy rats (4 months-old) stained with bisbenzimide to localize cell nuclei (red; *left panel*) and recoverin staining (white; *right panel*) to highlight both photoreceptor (pink arrows) and bipolar (green arrows) cell bodies. **b**, The frequency distribution of the cell diameter in non-dystrophic RCS-rdy retinas shows a bimodal pattern that allows distinguishing between photoreceptor (mean ± sem: 5.73 ± 0.78 μm) and bipolar (mean ± sem: 12.15 ± 0.14 μm) cell bodies. All 4 months-old dystrophic RCS groups, no matter whether treated (30 DPI) or untreated, show a single distribution of cell diameters around 12 μm, coinciding with that of bipolar cells in RCS-rdy. This shows that photoreceptors are dramatically decreased in all groups of RCS rats, while recoverin-positive bipolar cells are relatively unaffected. **c**, Pie charts representing the relative number of recoverin-positive photoreceptors and recoverin positive-bipolar cells expressed in percentage of the total cell body counts in control RCS-rdy retinas. The white areas in the RCS groups represent the percentage of photoreceptor loss. Sample size in **b,c** (experimental animals): n = 5 per experimental group (30 DPI). For each animal, images were acquired from corresponding fields in the various retinas by taking the injection site as reference point (2 slices/retina; 3 fields/slice). ONL, outer nuclear layer; INL, inner nuclear layer; GCL, ganglion cell layer. Scale bar, 50 μm.

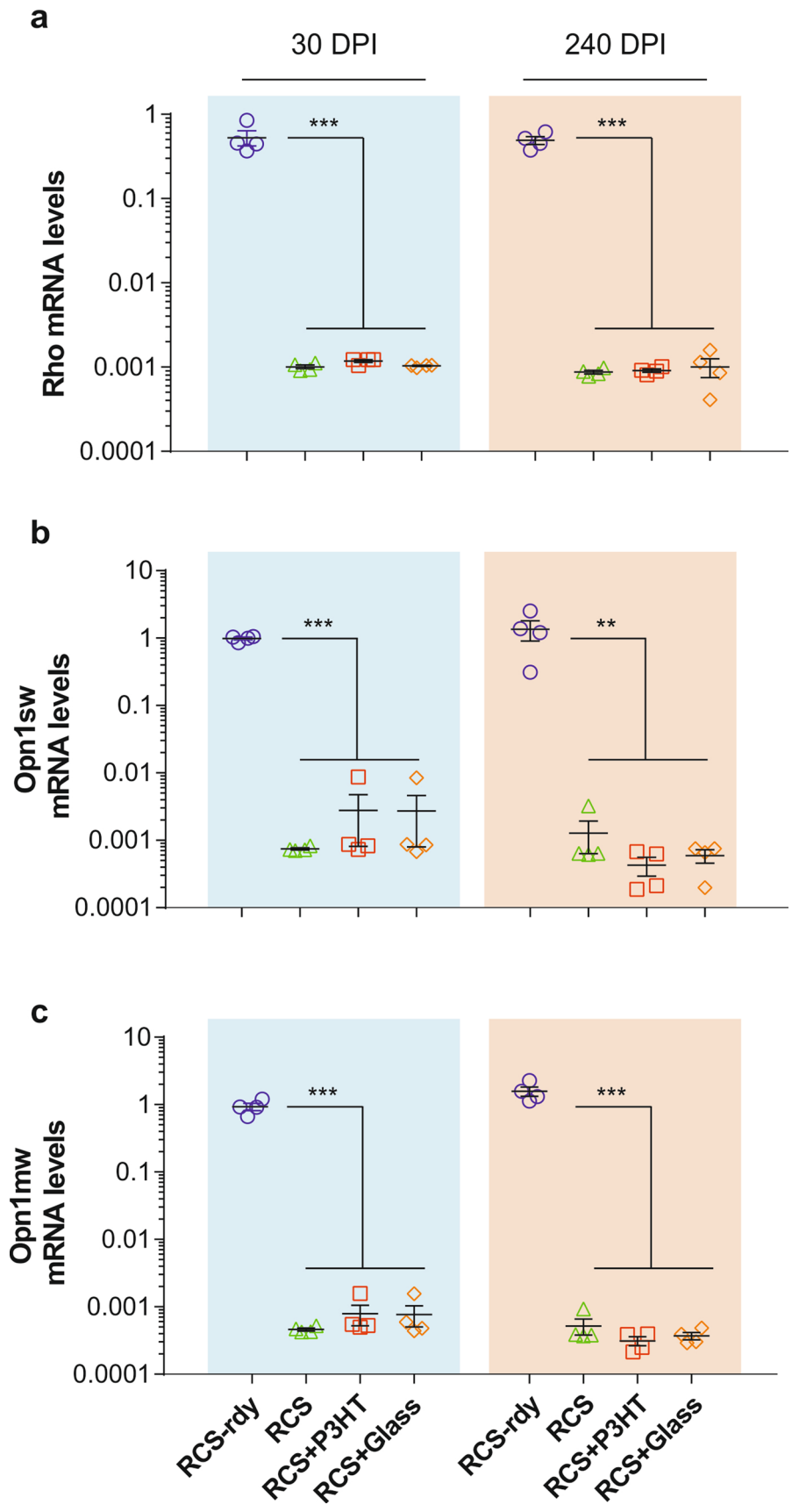

Extended Data Fig. 4 | See next page for caption.

Extended Data Fig. 4 | Expression of photoreceptor-specific mRNAs in the retina of RCS rats at 30 and 240 DPI. The mRNA levels of Rhodopsin (*Rho*; **a**), Opsin-1 short wave-sensitive (*Opn1sw*; **b**) and Opsin-1 medium wave-sensitive (*Opn1mw*; **c**) were quantified by qRT-PCR in retinal sections dissected from non-dystrophic controls (RCS-rdy) and dystrophic RCS rats that were non-injected (RCS) or injected with either P3HT-NPs or control Glass-NPs at 30 and 240 DPI. *Gapdh* and *HPRT1* were used as control housekeeping genes. Graphs show means ± sem on a semilogarithmic scale with superimposed individual points. Sample size (experimental animals): RCS-rdy (blue), n = 4; RCS (green), n = 4; RCS + P3HT (red), n = 4; RCS + Glass (orange), n = 4 for 30 and 240 DPI groups. $^{**}p < 0.01$, $^{***}p < 0.0001$, one-way ANOVA/Newman-Keuls tests *vs* the respective RCS-rdy group. For exact p values, see Supplementary Table 3.

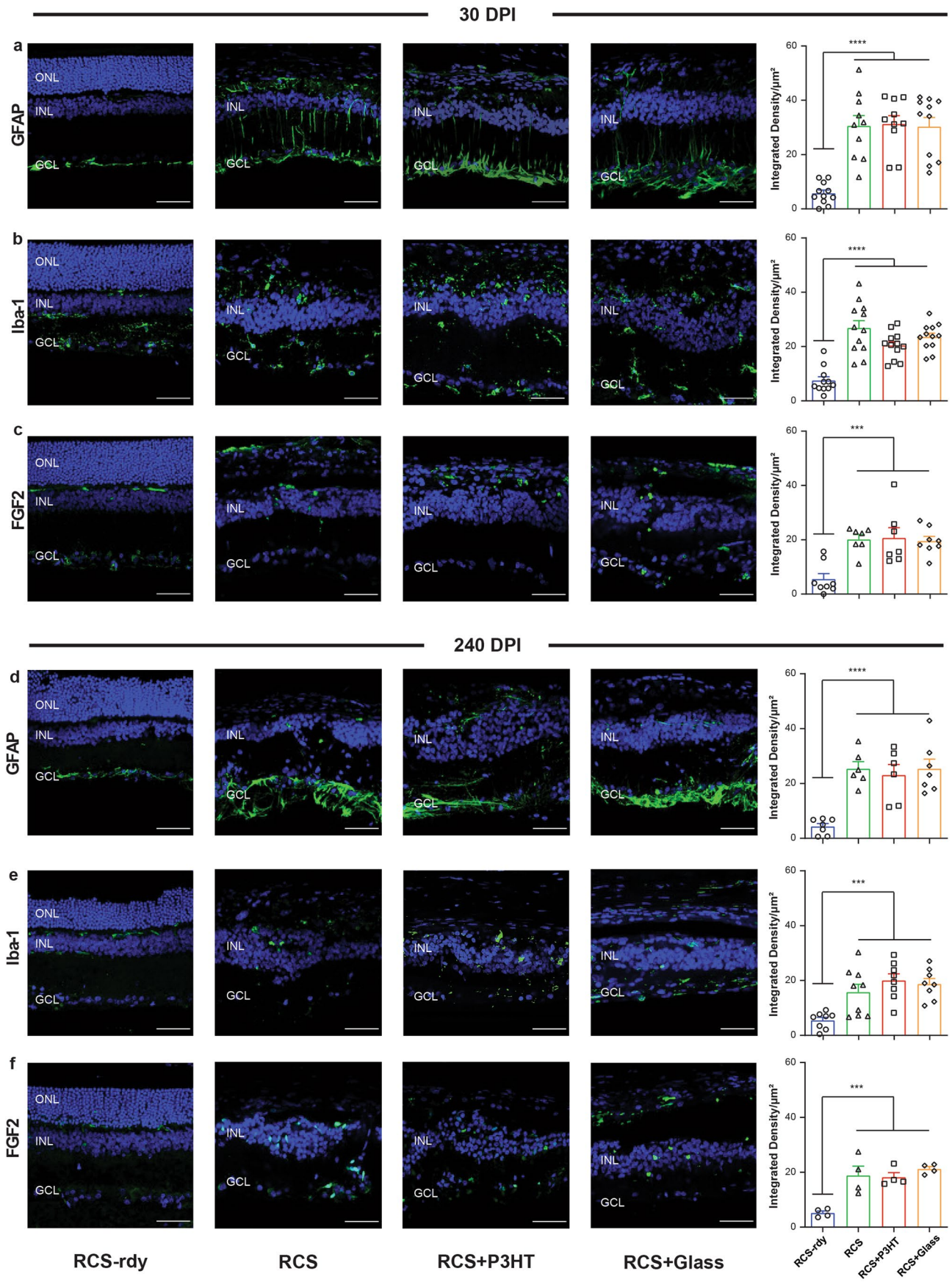

Extended Data Fig. 5 | See next page for caption.

Extended Data Fig. 5 | P3HT nanoparticles do not promote proinflammatory effects in dystrophic retinas. Transversal sections of representative retinas dissected at 30 DPI (**a–c**) and 240 DPI (**d–f**) from healthy controls (RCS-rdy) and dystrophic RCS rats that were untreated (RCS) or injected with either P3HT-NPs (RCS + P3HT) or control Glass-NPs (RCS + Glass). Sections were immunolabelled for: the astrocyte/Müller cell marker GFAP (**a,d**), the microglial marker Iba-1 (**b,e**) and the retinal trophic factor FGF2 (**c,f**). Images were acquired from corresponding fields in the various retinas by taking the injection site as reference point (2 slices/retina; 3 fields/slice). Immunostainings were merged with bisbenzimide nuclear labelling (blue). The bar plots on the right (means±sem with superimposed individual data points) report the quantitative analysis of the integrated fluorescence intensity. Dystrophic retinas display higher densities of activated astrocytes, microglial cells and FGF2-positive cells compared to RCS-rdy, as a result of the ongoing degeneration. All the RCS groups show a similar density of GFAP/Iba-1/FGF2 positive cells demonstrating that the presence of either P3HT-NPs or Glass-NPs did not promote a significant tissue inflammatory reaction. *** $p < 0.001$, **** $p > 0.0001$, *vs* RCS-rdy controls; one-way ANOVA/Dunnett's tests. Sample size (experimental animals) @ 30 DPI: GFAP 11, 10, 10, 11; Iba-1 11, 12, 12, 12; FGF2 8, 7, 7, 8; for RCSrdy, RCS, RCS + P3HT and RCS + Glass, respectively. Sample size (experimental animals) @ 240 DPI: GFAP 7, 6, 6, 7; Iba-1 8, 9, 8, 8; FGF2 4, 4, 4, 4; for RCSrdy, RCS, RCS + P3HT and RCS + Glass, respectively). For exact p values, see Supplementary Table 3. ONL, outer nuclear layer; INL, inner nuclear layer; GCL, ganglion cell layer. Scale bar, 50 μm.

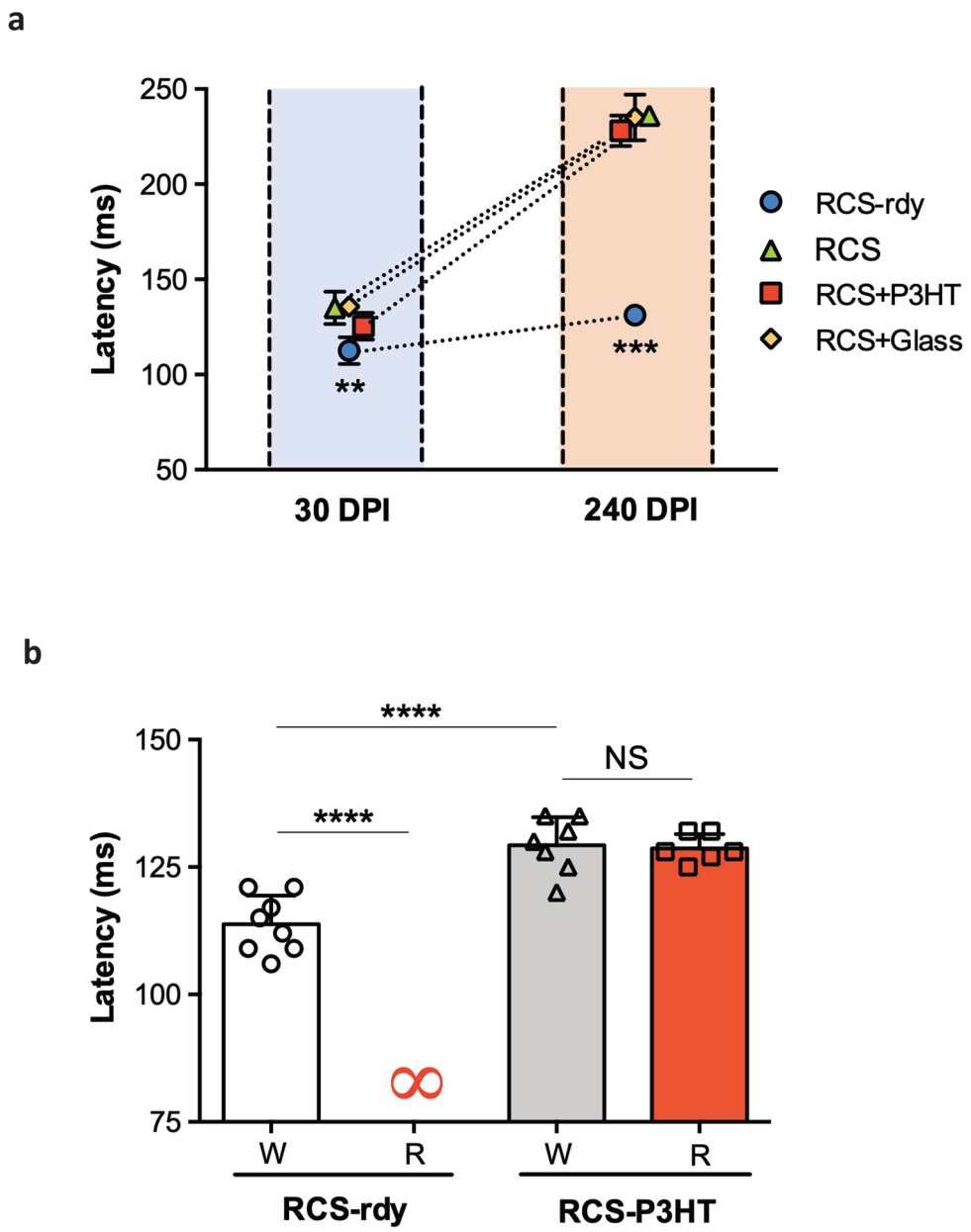

Extended Data Fig. 6 | VEP latency in RCS rats. a, Latency of VEPs evoked by white light flashes at 30 and 240 DPI. The electrophysiological analysis revealed that the VEP latency in RCS-rdy animals was significantly lower compared to that of RCS, RCS + P3HT-NPs or RCS + Glass-NPs at 30 DPI. The same phenomenon, albeit more pronounced, was observed at 240 DPI. The greatly increased VEP latency in aged dystrophic RCS rats is likely due to the extensive retinal rewiring that follows photoreceptor degeneration. Notably, the increased latency of dystrophic RCS rats is not rescued by P3HT-NPs at both 30 and 240 DPI. Data are means±sem. ** $p < 0.01$; *** $p < 0.001$ *vs* RCS-rdy controls at 30 and 240 DPI, respectively; one-way ANOVA/Tukey's tests. Sample size (experimental animals) @ 30 DPI: RCS-rdy, n = 8; RCS, n = 7; RCS + P3HT-NPs, n = 12; RCS + Glass-NPs, n = 6. Sample size (experimental animals) @ 240 DPI: n = 4 per each experimental group. **b**, Latency of VEPs evoked by white (W) or red (R) light flashes at 30 DPI from the experiment shown in Fig. 5h. No V1 response to red stimuli was detected in healthy RCS-rdy rats (indicated as infinite latency). The VEP latencies to white and red light of dystrophic RCS rats injected with P3HT-NPs were not significantly different, while they were both significantly longer that the VEP latency to white light of healthy RCS-rdy rats. **** $p < 0.0001$; NS $p > 0.05$; one-way ANOVA/Tukey's tests. Data are means±sem with superimposed individual experimental points. Sample size (experimental animals): RCS-rdy, n = 8; RCS + P3HT-NPs, n = 7. For exact p values, see Supplementary Table 3.

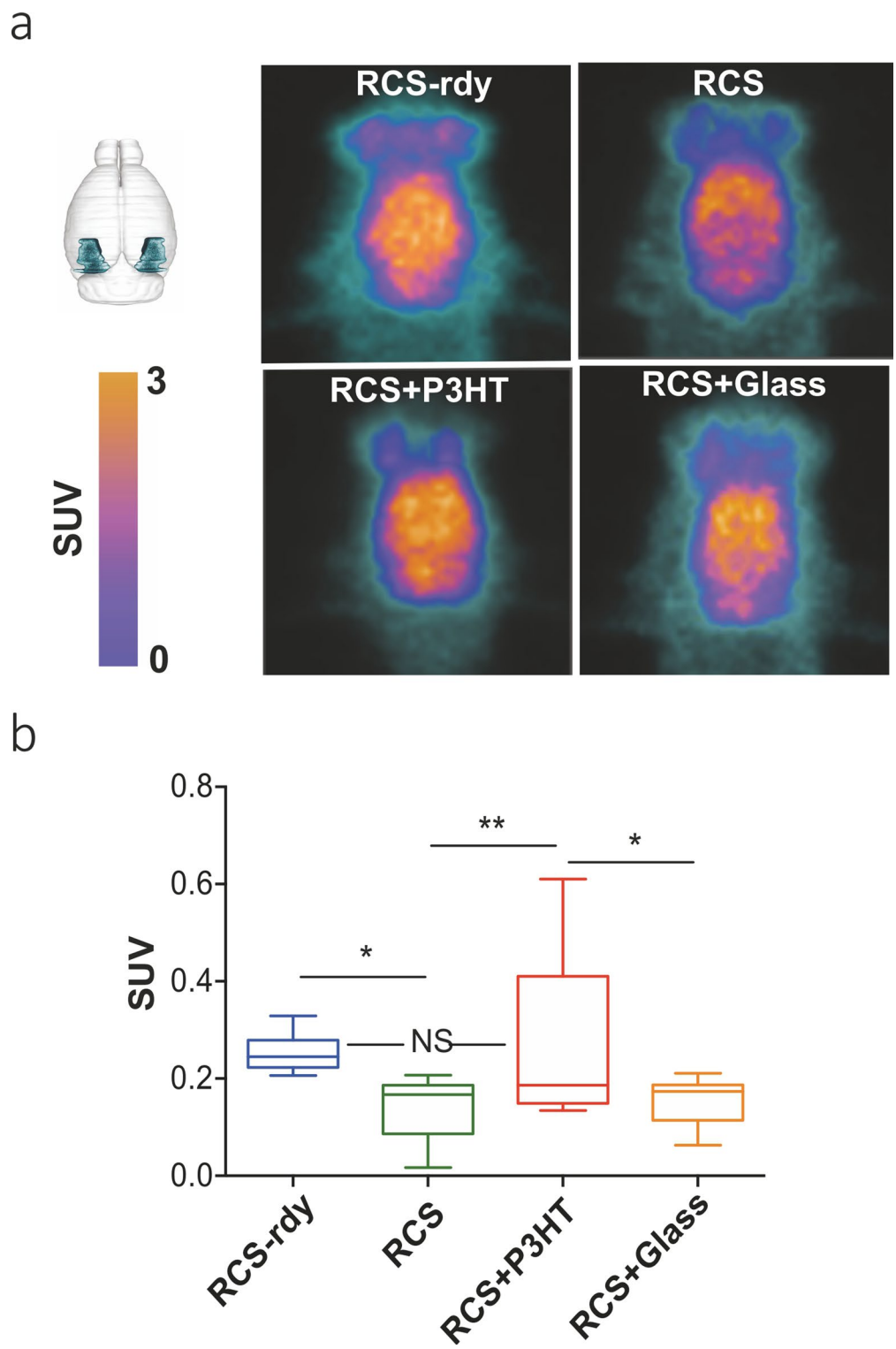

Extended Data Fig. 7 | Light-evoked metabolic activation of V1 is rescued in dystrophic RCS rats injected with P3HT nanoparticles. a, Representative brain images of basal metabolic activity acquired in the four experimental groups at 240 DPI. A map of the rat brain showing the location of V1 (blue areas) and a pseudo-colour scale corresponding to the average SUV of ^{18}F-FDG uptake over the scanned areas are shown on the left. **b**, Quantitative analysis of the average SUV in the V1 volumes of interest (~1 mm^3) demonstrates a significant increase in light evoked V1 metabolic activity in RCS rats injected with P3HT-NPs at 240 DPI. Box plots in **b** represent the median (centre line), mean (square), 25th-75th percentiles (box) and the limit of 3-fold the interquartile range. * $p < 0.05$; ** $p < 0.01$; one-way ANOVA/Tukey's tests. Sample size (experimental animals): RCS-rdy, n = 10; RCS, n = 12; RCS + P3HT-NPs, n = 14; RCS + glass-NPs, n = 11. For exact p values, see Supplementary Table 3.

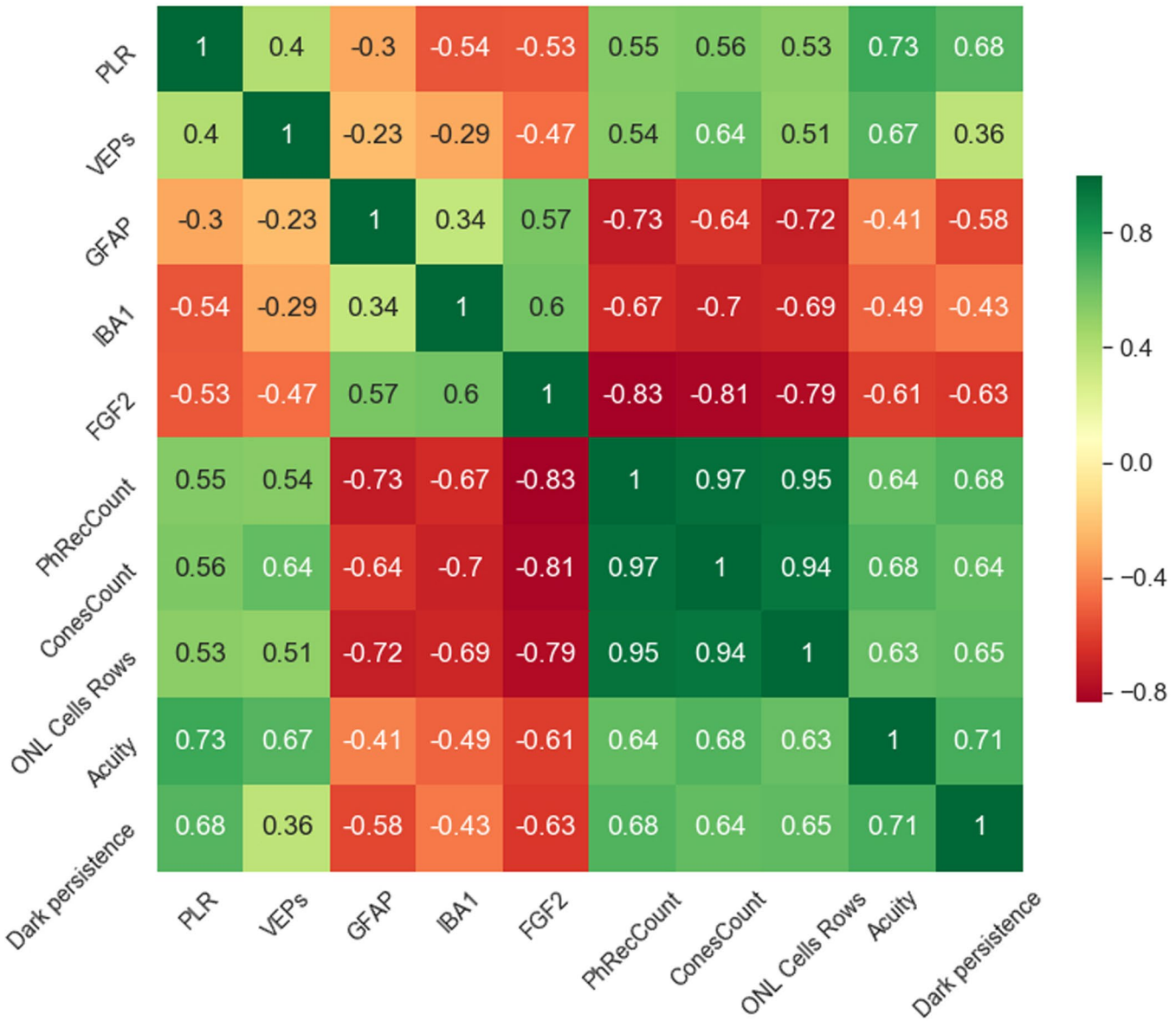

Extended Data Fig. 8 | Correlation map of all the variables studied in the four experimental groups of RCS rats. Each column and each row describe a different variable, with squares on the map representing the correlation between row and column variables ("photoreceptor", "inflammation" and "visual function" variables). Analysis by the Pearson's correlation coefficient revealed the existence of a strong correlation among all the variables, suggesting the use of a Principal Component Analysis decomposition. Sample size (experimental animals) @ 30 DPI: RCS-rdy, n = 5; RCS, n = 5; RCS + P3HT-NPs, n = 5; RCS + Glass-NPs, n = 6. Sample size (experimental animals) @ 240 DPI: RCS-rdy, n = 4; RCS, n = 4; RCS + P3HT-NPs, n = 4; RCS + Glass-NPs, n = 4. PLR, pupillary constriction; VEPs, VEP amplitude; GFAP, astrocyte immunoreactivity; IBA-1, microglia immunoreactivity; FGF2, fibroblast growth factor immunoreactivity; PhRecCounts, recoverin-positive photoreceptor cell bodies; ConesCounts, cone arrestin-positive cone cell bodies; ONL cell rows, bisbenzimide-stained nuclear rows in the ONL; Acuity, visual acuity; Dark persistence, percentage time in the dark in the light–dark box behavioural test.

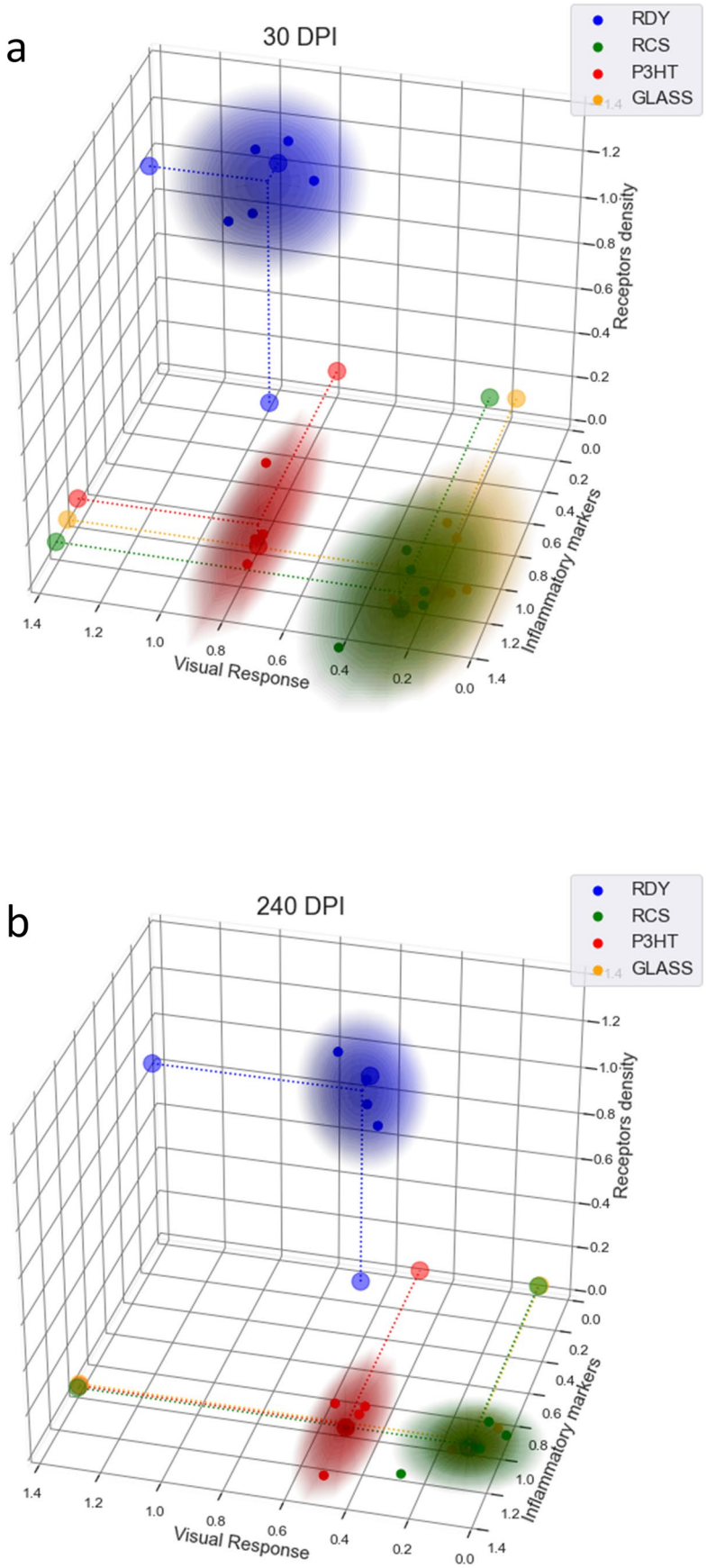

Extended Data Fig. 9 | See next page for caption.

Extended Data Fig. 9 | Component analysis for morphological and functional parameters in individual animals at 30 and 240 DPI. 3D plot of RCS morphological and functional parameters as a function of 3 reduced variables at 30 and 240 DPI. The x, y, z variables are indicators of visual performances (PLR, VEPs, Acuity, Dark persistence), photoreceptor cell counts (rod, cone and cell rows in the ONL, as reported in Supplementary Fig. 14) and the inflammatory state of the retina (GFAP, Iba-1 and FGF2 immunoreactivities, as reported in Supplementary Fig. 15), respectively. The scatter plots report the individual responses at 30 (**a**) and 240 (**b**) DPI within the four experimental groups. The shaded areas represent the highest values (up to 0.001) of the probability density function of the calculated clusters. The dashed lines and their terminal points represent the projections of each cluster centroid onto the origin planes. Sample size (experimental animals) @ 30 DPI: RCS-rdy (blue; n = 5), RCS (green; n = 5), RCS + P3HT-NPs (red; n = 5) and RCS + Glass-NPs (orange; n = 6). Sample size (experimental animals) @ 240 DPI: RCS-rdy (blue; n = 4), RCS (green; n = 4), RCS + P3HT-NPs (red; n = 4) and RCS + Glass-NPs (orange; n = 4).

nature research

Corresponding author(s): FABIO BENFENATI

Last updated by author(s): 14/04/20

Reporting Summary

Nature Research wishes to improve the reproducibility of the work that we publish. This form provides structure for consistency and transparency in reporting. For further information on Nature Research policies, see Authors & Referees and the Editorial Policy Checklist.

Statistics

For all statistical analyses, confirm that the following items are present in the figure legend, table legend, main text, or Methods section.

n/a	Confirmed	
☐	☒	The exact sample size (*n*) for each experimental group/condition, given as a discrete number and unit of measurement
☐	☒	A statement on whether measurements were taken from distinct samples or whether the same sample was measured repeatedly
☐	☒	The statistical test(s) used AND whether they are one- or two-sided *Only common tests should be described solely by name; describe more complex techniques in the Methods section.*
☒	☐	A description of all covariates tested
☐	☒	A description of any assumptions or corrections, such as tests of normality and adjustment for multiple comparisons
☐	☒	A full description of the statistical parameters including central tendency (e.g. means) or other basic estimates (e.g. regression coefficient) AND variation (e.g. standard deviation) or associated estimates of uncertainty (e.g. confidence intervals)
☐	☒	For null hypothesis testing, the test statistic (e.g. *F*, *t*, *r*) with confidence intervals, effect sizes, degrees of freedom and *P* value noted *Give P values as exact values whenever suitable.*
☒	☐	For Bayesian analysis, information on the choice of priors and Markov chain Monte Carlo settings
☒	☐	For hierarchical and complex designs, identification of the appropriate level for tests and full reporting of outcomes
☐	☒	Estimates of effect sizes (e.g. Cohen's *d*, Pearson's *r*), indicating how they were calculated

Our web collection on statistics for biologists contains articles on many of the points above.

Software and code

Policy information about availability of computer code

Data collection	Electrophysiological data were collected using the following softwares: Patch-clamp, Patchmaster V2.73 and FitMaster v2x90.1 (HEKA Elektronik); MEA, MC Rack V 4.6.2 (Multi Channel Systems). No commercial softwares were used to collect the other experimental data.
Data analysis	Prism 6.07 (Graphpad), OriginPro 9 (OriginLab), Python 3.1 , ImageJ (NIH), Matlab (MathWorks), Eye Explorer 3.2.1.0 (Spectralis)

For manuscripts utilizing custom algorithms or software that are central to the research but not yet described in published literature, software must be made available to editors/reviewers. We strongly encourage code deposition in a community repository (e.g. GitHub). See the Nature Research guidelines for submitting code & software for further information.

Data

Policy information about availability of data

All manuscripts must include a data availability statement. This statement should provide the following information, where applicable:

- Accession codes, unique identifiers, or web links for publicly available datasets
- A list of figures that have associated raw data
- A description of any restrictions on data availability

The experimental data that support the figures within this paper and other findings of this study are hosted at the Istituto Italiano di Tecnologia and can be accessed by contacting the corresponding author.

Field-specific reporting

Please select the one below that is the best fit for your research. If you are not sure, read the appropriate sections before making your selection.

☒ Life sciences ☐ Behavioural & social sciences ☐ Ecological, evolutionary & environmental sciences

For a reference copy of the document with all sections, see nature.com/documents/nr-reporting-summary-flat.pdf

Life sciences study design

All studies must disclose on these points even when the disclosure is negative.

Sample size	The number of mice necessary for the project was calculated based on: (i) experimental variability and need to reach a sufficient number of replications for a robust statistical analysis; (ii) duration of the project; (iii) occasional loss of animals due to anesthesia or unpredictable factors. Sample size (n) was predetermined using the following formula: n = Z2 × σ2 /Δ2, where: Z is the value of the distribution function f(α,β) (with α and β type-I and type-II errors, respectively) σ is the standard deviation of the groups, and Δ the minimum percent difference that is thought to be biologically relevant. By setting Z = 1.96 (based on α = 0.05 and 1-β=0.9), and Δ = 0.2 (20%) and σ ranging between 0.2-03 based on similar experiments and preliminary data, we calculated the total number of animals needed in the various experiments. for the planned experiments.
Data exclusions	No data exclusion was performed for in vitro/ex vivo data. For in vivo injected animals, treated animals (subretinal injection) that displayed retina detachment or breakage (OCT analysis) or cataract were preliminarly excluded from the analyses.
Replication	There were no findings that were not reproduced across distinct experimental sessions. Reproducibility of the data was assessed by statistically evaluating the intraexperimental and interexperimental variability.
Randomization	Two congenic rat strains (same genetic background) were used: RCS-rdy, used as the reference healthy control, and dystrophic RCS rats that were randomized among the three distinct experimental groups of non-injected, sham-injected (glass NPs) and injected (P3HT-NPs).
Blinding	Experiments were carried out blinded to the experimenter.

Reporting for specific materials, systems and methods

We require information from authors about some types of materials, experimental systems and methods used in many studies. Here, indicate whether each material, system or method listed is relevant to your study. If you are not sure if a list item applies to your research, read the appropriate section before selecting a response.

Materials & experimental systems

n/a	Involved in the study
☐	☒ Antibodies
☐	☒ Eukaryotic cell lines
☒	☐ Palaeontology
☐	☒ Animals and other organisms
☒	☐ Human research participants
☒	☐ Clinical data

Methods

n/a	Involved in the study
☒	☐ ChIP-seq
☒	☐ Flow cytometry
☒	☐ MRI-based neuroimaging

Antibodies

Antibodies used	Primary antibodies: goat polyclonal anti-Iba1 (1:500; ThermoFischer), mouse monoclonal anti-GFAP (1:200; Sigma Aldrich), mouse monoclonal anti-rhodopsin (1:100; Invitrogen), rabbit polyclonal anti-cone arrestin (1:250; Merck Millipore), rabbit polyclonal anti-recoverin (1:1000; Merck Millipore) and mouse monoclonal anti-FGF2 (1:150; Merck Millipore). Secondary antibodies: Alexa Fluor 488-conjugated or Alexa Fluor 637-conjugated anti-mouse, anti-rabbit and anti-goat secondary antibodies (Molecular Probes, Invitrogen).
Validation	Each primary antibody was validated in preliminary experiments for species and specificity of the immunostaining, also relying on the manufarturer's specifications, instructions and provided references.

Eukaryotic cell lines

Policy information about cell lines

Cell line source(s)	HEK293 cells from ATCC (CRL-1573).
Authentication	Identity of the cell lines was confirmed by Short Tandem Repeat (STR) profiling.

Mycoplasma contamination	Cells were routinely tested for mycoplasma and were negative.
Commonly misidentified lines (See ICLAC register)	N/A

Animals and other organisms

Policy information about studies involving animals; ARRIVE guidelines recommended for reporting animal research

Laboratory animals	Rat colonies (Royal College of Surgeons rats, healthy congenic strain RCS-rdy and dystrophic congenic strain RCS for in vivo and ex vivo studies) were bred under standard conditions with ad libitum access to food and water under a 12/12 h light/dark cycle. For in vitro studies, primary neurons were obtained from E18 Sprague-Dawley rat embryos of either sex.
Wild animals	The study did not involve wild animals.
Field-collected samples	The study did not involve samples collected from the field.
Ethics oversight	All animal manipulations and procedures were performed in accordance with the guidelines established by the European Community Council (Directive 2012/63/EU of 22 September 2010) and were approved by the Italian Ministry of Health (Authorization # 645/2015-PR).

Note that full information on the approval of the study protocol must also be provided in the manuscript.